

# 1 Isotopic composition of convective rainfall in the inland tropics of 2 Brazil

3 Vinicius dos Santos<sup>1</sup>, Didier Gastmans<sup>1</sup>, Ana María Durán-Quesada<sup>2</sup>, Ricardo Sánchez-Murillo<sup>3</sup>,  
4 Kazimierz Rozanski<sup>4</sup>, Oliver Kracht<sup>5</sup> and Demilson de Assis Quintão<sup>6</sup>.

5

6 <sup>1</sup>São Paulo State University (UNESP), Environmental Studies Center. Av. 24A, 1515, Bela Vista, 13.506-900, Rio Claro, São  
7 Paulo, Brazil. [vinicius.santos16@unesp.br](mailto:vinicius.santos16@unesp.br); [didier.gastmans@unesp.br](mailto:didier.gastmans@unesp.br)

8 <sup>2</sup>Escuela de Física & Centro de Investigación en Contaminación Ambiental & Centro de Investigaciones Geofísicas,  
9 Universidad de Costa Rica, San José 11501, Costa Rica. [ana.duranquesada@ucr.ac.cr](mailto:ana.duranquesada@ucr.ac.cr)

10 <sup>3</sup>University of Texas at Arlington, Department of Earth and Environmental Sciences, 500 Yates Street, Arlington, Texas 76019,  
11 USA. [ricardo.sanchezmurillo@uta.edu](mailto:ricardo.sanchezmurillo@uta.edu)

12 <sup>4</sup>Faculty of Physics and Applied Computer Science, AGH University of Krakow, al. Mickiewicza 30, 30-059 Krakow, Poland.  
13 [rozanski@agh.edu.pl](mailto:rozanski@agh.edu.pl)

14 <sup>5</sup>International Atomic Energy Agency, Isotope Hydrology Section, Vienna International Centre, P. O. Box 100, 1400 Vienna,  
15 Austria. [O.Kracht@iaea.org](mailto:O.Kracht@iaea.org)

16 <sup>6</sup>São Paulo State University (UNESP), IPMet/Science College, Est. Mun. José Sandrin IPMET, S/N, 17.048-699, Bauru, São  
17 Paulo, Brazil. [demilson.quintao@unesp.br](mailto:demilson.quintao@unesp.br)

18

19 *Correspondence to:* Didier Gastmans ([didier.gastmans@unesp.br](mailto:didier.gastmans@unesp.br))

20 **Abstract.** The tropical central-southern region of Brazil is characterized by strong convective systems. These systems provide  
21 abundant water for agro-industrial activities but also pose flood risks to large cities. Here, we present high-frequency (2-10  
22 min) rainfall isotopic compositions (n=90 samples) to reveal the regional and local atmospheric processes controlling the  
23 isotopic variability of convective systems from 2019-2021. Isotope parameters from individual events, including initial ( $\delta_{\text{initial}}$ ),  
24 median ( $\delta_{\text{med}}$ ), and the difference between lowest and highest isotope values ( $\Delta\delta$ ), and detailed meteorological data, were used  
25 in inter-event and intra-event analysis. The lower  $\delta_{\text{initial}}$  values were associated with higher rainfall along Hysplit trajectories  
26 from the Amazon forest during the summer, compared to autumn and spring, when Hysplit trajectories from the Atlantic Ocean  
27 and South Brazil had lower amounts of rainfall. Consequently, there were high  $\delta_{\text{initial}}$  values. This regional  $\delta$ -signature was  
28 conserved during certain convective intra-events, with similar values between the  $\delta_{\text{initial}}$  and  $\delta_{\text{median}}$ . However, for other intra-  
29 events, the  $\delta_{\text{initial}}$  values were altered by local processes connected to cloud features, rainfall vertical structure, and humidity  
30 conditions, resulting in increased isotopic variations ( $\Delta\delta$ ) during intra-events. Our findings establish a novel framework for  
31 evaluating the meteorological controls on the isotopic variability of convective precipitation in tropical South America, fill the  
32 gap of high-frequency studies in this region, and generate a comprehensive meteorological dataset for future modeling studies.

## 33 1 Introduction

34 The tropical central-southern region of Brazil (CSB) is the primary contributor to the country's economy, with agriculture and  
35 agroindustry as the main sectors (Zilli et al., 2017). These economic activities are highly dependent on seasonal rainfall for  
36 irrigation and hydropower supply (Luiz Silva et al., 2019). Projected changes in the frequency of heavy and extreme rainfall  
37 events in future climate scenarios (Marengo et al., 2020; Donat et al., 2013; IPCC, 2021; Marengo et al., 2021) pose a  
38 significant threat to regional economic enterprises and power generation. Similarly, according to Marengo et al. (2021),  
39 simulations with the pre-CMIP6 models suggest that the intensification of heavy rainfall events could exacerbate the  
40 prevalence of floods and landslides in susceptible regions. Such occurrences have resulted in a total cost of US\$41.7 billion  
41 over the past half-century (Marengo et al., 2020; World Meteorological Organization, 2021).

42 Extreme precipitation events are linked to convective systems (CS). The CS significantly contribute proportion of annual  
43 rainfall and account for a significant portion of extreme rainfall (Roca and Fiolleau, 2020). Across the tropics, diurnal surface  
44 heating amplifies convection, generating short-lived events that can occur in consecutive days. Rapid upward movement of air  
45 results in quick condensation and formation of precipitation with substantial droplets and heavy rainfall (Breugem et al., 2020;  
46 Kastman et al., 2017; Lima et al., 2010; Machado et al., 1998). This is identified by vigorous vertical development in the form  
47 of *cumulus-nimbus* and *cumulus congestus* (convective clouds) and low-level divergence (stratiform clouds) (Siqueira et al.,  
48 2005; Machado and Rossow, 1993; Zilli et al., 2017; Houze, 1989, 2004). Precipitation associated with these systems are  
49 commonly referred as convective and stratiform rainfall, and account for 45% and 46% of the total rainfall in South America,  
50 respectively (Romatschke and Houze, 2013).

51 Whether rainfall is convective or stratiform rainfall has been suggested to determine variations in stable isotope  
52 composition of precipitation across the tropics (Zwart et al., 2018; Sánchez-Murillo et al., 2019; Sun et al., 2019; Han et al.,  
53 2021; Aggarwal et al., 2016; Munksgaard et al., 2019).

54 Processes driving the variations in the isotopic composition in convective systems are more complex and less understood  
55 compared to the case of other precipitation producing systems (de Vries et al., 2022). Studies using the isotopic composition  
56 of rain and water vapor have quantified and modelled physical processes related to convection (Bony et al., 2008; Kurita,  
57 2013). Previous studies have suggested that the isotopic composition of convective systems is connected to the integrated  
58 history of convective activity (Risi et al., 2008; Moerman et al., 2013), depth of organized convection and aggregation  
59 (Lawrence et al., 2004; Lekshmy et al., 2014; Lacour et al., 2018; Galewsky et al., 2023), microphysical processes within  
60 clouds (Aggarwal et al., 2016; Lawrence et al., 2004; Zwart et al., 2018), and cold pool dynamics (Torri, 2021). These  
61 interpretations simplified and lumped the effects of multiple rainfall timescales (e.g. monthly, daily and high frequency),  
62 providing different perspectives on convective processes, such as the regional (synoptic forcings) and local factors (e. g.  
63 microphysical processes occurring both within and below the cloud) (Kurita et al., 2009; Muller et al., 2015).

64 High-frequency rainfall sampling and analyses of stable isotope ratios has been used to better understand the evolution of  
65 large weather systems such as tropical cyclones and typhoons (Sun et al., 2022; Sánchez-Murillo et al., 2019; Han et al., 2021),

66 squall lines (Taupin et al., 1997; Risi et al., 2010; Tremoy et al., 2014) and local evaporation effects (Graf et al., 2019;  
67 Aemisegger et al., 2015; Lee and Fung, 2008). High-resolution isotope information can provide a better insight into the  
68 development of weather systems and cloud dynamics, both responsible for changes in the rain type, intensity, and inherent  
69 isotope variability during the life cycle of rainfall events (Coplen et al., 2008; Muller et al., 2015; Celle-Jeanton et al., 2004).

70 In this study, we used high-frequency rainfall sampling to investigate regional (moisture origin/transport, regional  
71 atmospheric circulation) and local (below-cloud processes, vertical structure of rainfall, cloud top temperature) processes that  
72 controlling the isotopic composition of convective rainfall. High-frequency rainfall was integrated with ground-based  
73 observational data (Micro Rain Radar and automatic weather station), satellite imagery (GOES-16), ERA-5 reanalysis  
74 products, and HYSPLIT trajectories to better characterize convective rainfall over the inland tropics of Brazil.

## 75 **2 Data and Methods**

### 76 **2.1 Sampling site and weather systems**

77 The rainfall sampling site was localized in Rio Claro city, São Paulo State (Fig. 1a). The station (-22.39°S, -47.54°W, 670 m  
78 a.s.l.) is part of the Global Network of Isotopes in Precipitation network (GNIP) and is influenced by weather systems  
79 responsible for rainfall variations and seasonality linked to the regional atmospheric circulations across the CSB region. The  
80 rainfall seasonality over CSB is associated with: (i) frontal systems (FS), represented mainly by cold fronts from southern  
81 South America acting throughout the year, and (ii) the activity of the South Atlantic Convergence Zone (SACZ) during austral  
82 summer (December to March) (Kodama, 1992; Garreaud, 2000) (Fig. 1b). These features are mostly responsible for CS  
83 development (Romatschke and Houze, 2013; Siqueira et al., 2005; Machado and Rossow, 1993) (Fig. 1c), and were captured  
84 during their passage over the Rio Claro station.

### 85 **2.2 Rainfall sampling and isotope analyses**

86 High-frequency rainfall sampling was conducted using a passive collector (2 to 10 minutes intervals) from September 2019 to  
87 February 2021, except for April, July, and August (during winter 2020), when no rainfall was observed in the study area. The  
88 pandemic Covid-19 disrupted access to the university, thereby reducing the number of rainfall events sampled during the  
89 spring of 2020, particularly at night (e.g., lockdowns). In this study, the rainfall samples collected do not consist of consecutive  
90 day-night pairs during the same day. In total, 90 samples representing eight convective events (3 night-time and 5 day-time  
91 events) were collected. Samples were transferred to the laboratory and stored in 20 mL HDPE bottles at 4 °C. In parallel to  
92 high-frequency sampling, monthly cumulative rainfall samples were also collected at the Rio Claro site during the study period  
93 as a contribution to the GNIP network, using the methodology recommended by the International Atomic Energy Agency  
94 (IAEA, 2014).

95 Rainfall samples were analyzed for stable isotope composition using Off-Axis Integrated Cavity Output Spectroscopy (Los  
96 Gatos Research Inc.) at the Hydrogeology and Hydrochemistry laboratory of UNESP's Department of Applied Geology and  
97 at the Chemistry School of the National University (UNA, Heredia, Costa Rica). All results are expressed in per mil relative  
98 to Vienna Standard Mean Ocean Water (V-SMOW). The certified calibration standards used in UNESP were USGS-45 ( $\delta^2\text{H}$   
99 =  $-10.3$  ‰,  $\delta^{18}\text{O}$  =  $-2.24$  ‰), USGS-46 ( $\delta^2\text{H}$  =  $-236.0$  ‰,  $\delta^{18}\text{O}$  =  $-29.80$  ‰), including one internal standard (Cachoeira de  
100 Emas - CE –  $\delta^2\text{H}$  =  $-36.1$  ‰,  $\delta^{18}\text{O}$  =  $-5.36$  ‰). USGS standards were used to calibrate the results on the V-SMOW2-SLAP2  
101 scale, whereas CE was used for memory and drift corrections. At UNA, the certified standards MTW ( $\delta^2\text{H}$  =  $-130.3$  ‰,  $\delta^{18}\text{O}$   
102 =  $-16.7$  ‰), USGS45 ( $\delta^2\text{H}$  =  $-10.3$  ‰,  $\delta^{18}\text{O}$  =  $-2.2$  ‰), and CAS ( $\delta^2\text{H}$  =  $-64.3$  ‰,  $\delta^{18}\text{O}$  =  $-8.3$  ‰) were used to correct the  
103 measurement results for memory and drift effects and to calibrate them on the V-SMOW2-SLAP2 scale (García-Santos et al.,  
104 2022). The analytical uncertainty ( $1\sigma$ ) was  $1.2$  ‰ for  $\delta^2\text{H}$  and  $0.2$  ‰ for  $\delta^{18}\text{O}$  for UNESP analysis and  $0.38$  ‰ for  $\delta^2\text{H}$  and  
105  $0.07$  ‰ for  $\delta^{18}\text{O}$  for UNA analysis. Deuterium excess (*d*-excess) was calculated as:  $d\text{-excess} = \delta^2\text{H} - 8 \cdot \delta^{18}\text{O}$  (Dansgaard,  
106 1964), with uncertainties ( $1\sigma$ ) of  $1.33$  and  $0.43$  ‰, respectively. This secondary isotope parameter was used to interpret the  
107 influence of moisture origin/transport (Sánchez-Murillo et al., 2017; Froehlich et al., 2002) and local processes (Aemisegger  
108 et al., 2015; Muller et al., 2015; Celle-Jeanton et al., 2004).

### 109 **2.3 Meteorological data**

110 Automatic Weather Station (AWS) Decagon Em50 (METER) was installed near the Micro Rain Radar (MRR) (METEK) at  
111  $670$  m.a.s.l, in immediate vicinity of the rainfall collection site. Meteorological data were recorded at  $1$  min intervals for rain  
112 rate (RR,  $\text{mm min}^{-1}$ ), air temperature (T,  $^{\circ}\text{C}$ ) and relative humidity (RH, %). The MRR data for reflectivity (Zc, dBZ), and fall  
113 velocity (w,  $\text{m s}^{-1}$ ) were also recorded at  $1$  min intervals. MRR parameters correspond to the mean values measured at the  
114 elevation between  $150$  and  $350$  meters above surface. MRR operated at a frequency of  $24.230$  GHz, modulation of  $0.5 - 15$   
115 MHz according to the height resolution mode. For this work, different height resolutions ( $31$  range bin) were tested,  $150$  m,  
116  $200$  m,  $300$  m and  $350$  m, resulting in vertical profiles of  $4650$  m,  $6200$  m,  $9300$  m and  $10.850$  m, respectively (Endries et al.,  
117 2018). The MRR data used in the following discussion are the near-surface data (first measurement from  $150$  m to  $350$  m).  
118 Lifting Condensation Level (LCL, meters) was computed from AWS RH and T, using expression proposed by Soderberg et  
119 al. (2013) and rainfall amount (R, mm) was calculated during the sampling interval. GOES-16 imagery was used to identify  
120 the convective nuclei of the cloud-top ( $10.35\text{-}\mu\text{m}$ , Band-13) and brightness temperature (BT,  $^{\circ}\text{C}$ ), at  $10$  min intervals during  
121 the sampling period (Ribeiro et al., 2019; Schmit et al., 2017). The  $10.35\text{-}\mu\text{m}$  BT is often used to estimate the convective cloud  
122 depth, since the lower BT is linked to deeper cloud tops (Adler and Fenn, 1979; Roberts and Rutledge, 2003; Adler and Mack,  
123 1986; Ribeiro et al., 2019; Machado et al., 1998). The weather systems (fronts, instabilities, and low pressure) were defined  
124 according to the synoptic chart and meteorological technical bulletin of the Center for Weather Forecast and Climatic Studies  
125 of the National Institute of Space Research (CPTEC/INPE) that used information of numerical models, automatic weather

126 stations, satellite and radar images, reanalysis data and regional atmospheric models, such as the Brazilian Global Atmospheric  
127 Model and ETA model.

128

#### 129 **2.4 Hysplit modeling and Reanalysis data**

130 The origin of air masses and moisture transport to the Rio Claro site were evaluated using the HYSPLIT (Hybrid-Single  
131 Particle Lagrangian Integrated Trajectory) modeling framework (Stein et al., 2015; Soderberg et al., 2013). The trajectories of  
132 the air masses were estimated for 240 hours prior to rainfall onset, considering the estimated time of residence of the water  
133 vapor (Gimeno et al., 2010, 2020; van der Ent and Tuinenburg, 2017). Start time of trajectories was the same as the start time  
134 of rainfall events. The trajectories were computed using NOAA's meteorological data (global data assimilation system, GDAS:  
135 1 degree, global, 2006-present), with ending elevations of the trajectories at 1500 m above the surface, taking into account the  
136 climatological height of the Low Level Jet, within 1000–2000 m (Marengo et al., 2004). Ten-day trajectories representing  
137 convective events were calculated as trajectory ensembles, each consisting of twenty-seven ensemble members released at  
138 start hour of convective rainfall sample collection. Ensembles were produced by varying the initial trajectory wind speeds and  
139 pressures, according to the HYSPLIT ensemble algorithm, in order to account for the uncertainties involved in the simulation  
140 of individual backward trajectories (Jeelani et al., 2018). A sum of the rainfall intensity ( $\text{mm hr}^{-1}$ ) along the trajectories was  
141 used to analyse rainout of the moist air masses according to the Jeelani et al. (2018).

142 Reanalysis data were used to better understand the influence of atmospheric circulation on isotopic composition of rainfall  
143 at the study area. ERA-5 information was used to evaluate hourly vertical integrals of eastward water vapor flux ( $\text{kg m}^{-1} \text{s}^{-1}$ )  
144 during convective events sampled. The Global Modeling and Assimilation Office (GMAO) data (MERRA-2, 1 hour, 0.5 x  
145 0.625 degree, V5.12.4) were used for calculations of latent heat flux (LHF). Aqua/AIRS L3 Daily Standard Physical Retrieval  
146 (AIRS-only) data (1 degree x 1 degree V7.0, Greenbelt, MD, USA, Goddard Earth Sciences Data and Information Services  
147 Center) (known as GES DISC) were used for average outgoing longwave radiation (OLR). OLR values below  $240 \text{ W m}^{-2}$   
148 indicate organized deep convection (Gadgil, 2003).

#### 149 **2.5 Identification of convective rainfall events**

150 In general, identification of convective precipitation systems was based on the vertical structure of the given precipitation  
151 system (lack of the melting layer and bright band - BB) in the radar profiles featuring high reflectivity values ( $Z_c > 38 \text{ dBZ}$ )  
152 (Houze, 1993, 1997; Steiner and Smith, 1998; Rao et al., 2008; Mehta et al., 2020; Endries et al., 2018) and satellite imagery  
153 (Vila et al., 2008; Ribeiro et al., 2019; Siqueira et al., 2005; Machado et al., 1998). Consequently, convective rainfall was  
154 defined in this study by (i) convective cloud nuclei observed in GOES-16 imagery, (ii) no BB detected, (iii)  $Z_c > 38 \text{ dBZ}$  near  
155 to the surface and (iv) rainfall intensity (AWS) of at least  $10 \text{ mm h}^{-1}$  (Klaassen, 1988) (Fig. 1c,d). The convective nuclei were  
156 identified using GOES-16 imagery, determined as a contiguous area of at least 40 pixels with BT lower than  $235\text{K}$  ( $\leq -38 \text{ }^\circ\text{C}$ )  
157 over Rio Claro station, according to previous studies (Ribeiro et al., 2019).

158 **2.6 Preliminary assessment of local processes**

159 Below-cloud atmospheric conditions are known to be relevant and while we acknowledge that a more robust dataset is required  
 160 to provide sound conclusions, a preliminary assessment of this factor is herein included.

161 Since the isotopic composition of near-ground water vapor during the rainfall events was not measured, the framework  
 162 proposed by Graf et al. (2019) for interpreting below-cloud effects on rainfall isotopes cannot be applied here. A semi-  
 163 quantitative evaluation of those effects is demonstrated for all rainfall events, despite the need for a more substantial dataset  
 164 to establish firm conclusions. This analysis considers the following assumptions: (i) median values of isotope and  
 165 meteorological parameters recorded for each analysed event (Table 1) will be used in the calculations, (ii) linear interpolation  
 166 of air temperature and relative humidity between the cloud base level and the ground level will be adopted to estimate the  
 167 relative humidity at the cloud base ( $RH_{INT}$ ), (iii) it will be assumed that atmosphere is saturated with water vapour at the cloud  
 168 base level ( $RH = 100\%$ ), and (iv) the reservoir of water vapour below the cloud base level is isotopically homogeneous (Risi  
 169 et al., 2019; Sarkar et al., 2023).

170 Isotopic evolution of raindrops falling through unsaturated humid atmosphere beneath the cloud base level will be  
 171 calculated using the generally accepted conceptual framework for isotope effects accompanying evaporation of water into a  
 172 humid atmosphere (Craig and Gordon, 1965; Horita et al., 2008). Isotopic evolution of an isolated water body (e.g. falling  
 173 raindrop) evaporating into a humid atmosphere can be described by the following equations (Gonfiantini, 1986):

$$174 \quad \delta = \left( \delta_o - \frac{A}{B} \right) F^B + \frac{A}{B} \quad (1)$$

175 where

$$176 \quad A = \frac{h_N \delta_A + \varepsilon_{kin} + \varepsilon_{eq} / \alpha_{eq}}{1 - h_N + \varepsilon_{kin}} \quad (2)$$

177 and

$$178 \quad B = \frac{h_N - \varepsilon_{kin} - \varepsilon_{eq} / \alpha_{eq}}{1 - h_N + \varepsilon_{kin}} \quad (3)$$

179 Parameter  $F$  describes the remaining fraction of the evaporating mass of water (raindrop), while  $\delta_A$  stands for the isotopic  
 180 composition of ambient moisture. Initial and actual isotopic compositions of the evaporating water body, expressed in  $\delta$   
 181 notation, are represented by  $\delta_o$  and  $\delta$ , respectively. The variables in equations (3) and (4) are described as:

182  $h_N$  – relative humidity of the ambient atmosphere, normalized to the temperature of the evaporating water body;

183  $\alpha_{eq}$  – temperature-dependent equilibrium fractionation factor, derived from empirical equations proposed by Horita and  
 184 Wesolowski (1994);

185  $\varepsilon_{eq}$  – equilibrium fractionation coefficient:  $\varepsilon_{eq} = \alpha_{eq} - 1$  (4)

186  $\varepsilon_{kin}$  - kinetic fractionation coefficient;  $\varepsilon_{kin} = \alpha_{kin} - 1$  (5)

187 The kinetic fractionation coefficient is a linear function of the relative humidity deficit in the ambient atmosphere (Gat,  
 188 2001; Horita et al., 2008):

189  $\varepsilon_{kin} = n \cdot \varepsilon_{diff}(1 - h_N)$  (6)

190 where  $n$  describes a turbulence parameter, varying from zero to one and  $\varepsilon_{diff}$  is the kinetic fractionation coefficient associated  
191 with diffusion of water isotopologues in air.

192 The value of  $n$  is controlled mainly by wind conditions prevailing over the evaporating surface. It quantifies the apparent  
193 reduction of  $\varepsilon_{diff}$  due to the impact of turbulent transport. The value of  $n = 0.5$ , was adopted in the calculations, following the  
194 results of laboratory experiments with evaporation of water drops in a humid atmosphere reported by Stewart (1975).  
195 Following this same publication, the value of the F parameter for each event was computed based on the rate of change of  
196 evaporated drop radius as a function of ambient relative humidity (Stewart, 1975). Droplets with a drop size distribution of  
197 1mm are assumed based on previous studies in this region of study (Zawadzki and Antonio, 1988; Cecchini et al., 2014).  
198 Travel time of raindrops drops from the cloud base to the surface was derived from the position of LCL level and the terminal  
199 velocity of drops. It was further assumed in the calculations that the difference between drop temperature and ambient air  
200 temperature is small, thus allowing to use ambient humidity instead to normalized humidity. Although this assumption may  
201 result in an over-estimation of the impact of partial evaporation of raindrops on their isotope characteristics, the effect is  
202 expected to be small due to high ambient relative humidities (> 90 %) used in the calculations.

## 203 **2.7 Statistical tests**

204 The Shapiro-Wilk test was applied to verify that the data distribution was normal (parametric) or non-normal (non-parametric)  
205 (Shapiro, S. S.; Wilk, 1965). A significant difference (p-value < 0.05) indicates a non-parametric distribution. A Spearman  
206 rank correlation test was used for nonparametric distribution data, whereas Pearson's linear correlation test was applied for  
207 parametric data. Correlation tests were conducted between isotopes ( $\delta^{18}\text{O}$  and  $d$ -excess) and meteorological data (AWS and  
208 MRR variables) during the same time interval and from individual events. Correlation tests were not applied to GOES-16 BT  
209 and reanalysis data due to their temporal resolution, which reduced the number of samples. All tests were performed with  
210 significance levels defined by a p-value < 0.05, using the R statistical package (R Core Team, 2023).

211 A statistical analysis was carried out to characterize regional and local influences, in accordance with He et al. (2018). The  
212 initial isotope data of the events ( $\delta_{\text{initial}}$ ) closely reflects the initial air mass or vapor from which the precipitation originates.  
213 The  $\delta_{\text{initial}}$  and median ( $\delta_{\text{med}}$ ) values were employed to identify regional influences in inter-event analysis. Also, the difference  
214 ( $\Delta\delta$ ) between the lowest  $\delta^{18}\text{O}$  and the highest  $\delta^{18}\text{O}$  value represents the local change in  $\delta$ -value during the intra-event (Muller  
215 et al., 2015; He et al., 2018).

## 216 **3 Results**

### 217 **3.1 Isotopic and synoptic characteristics**

218 The isotopic composition of monthly rainfall exhibits clear seasonal variations between September 2019 and February 2021  
219 (Fig. 2a). Seasonal variability was characterized by wet (low  $\delta^{18}\text{O}$ ) and dry (high  $\delta^{18}\text{O}$ ) seasons (austral summer and autumn-  
220 spring, respectively). High-frequency sampling of convective events could not be done uniformly during the study period, but  
221 it is still evident that median  $\delta^{18}\text{O}$  values of high-frequency sampling events (black symbols in Fig. 2a) follow the seasonal  
222 isotope variability.

223 The summer months were characterized by the influence of convective activity, reflected in high latent heat flux and lower  
224 OLR (Fig. 2c). During autumn and spring, significant lower latent heat flux and higher OLR were associated with less  
225 convective development (Houze, 1997, 1989). The formation of convective rainfall may not be primarily controlled by diurnal  
226 thermal convection, as rainfall is more likely to be associated with frontal systems (Siqueira and Machado, 2004), as observed  
227 in the rainfall episodes during autumn and spring.

228 A significant influence of the cold fronts was observed before, during, and after their passage over the study area (Fig. 2a).  
229 During autumn and spring, the convective events of 2019/11/05, 2020/11/18, and 2020/05/23 were associated with cold fronts  
230 in the study area. On 2020/06/09, changes in the regional atmosphere over the state of São Paulo caused convective rainfall  
231 due to an instability (frontal) system resulting from a cold front settling over the southern region of Brazil. During the summer  
232 season, convective rainfall also occurred on 2020/02/01 and 2021/02/24 due to cold fronts and instability (frontal),  
233 respectively. In addition, the thermal convection of the continental region caused atmospheric ascent via surface heating in the  
234 inland of Brazil, leading to a system responsible for the convective rainfall event on 2020/01/30. As a result of the interaction  
235 between thermal convection and the incursion of the frontal system, a low-pressure system (frontal) was responsible for the  
236 convective rainfall event on 2020/02/10.

237 Table 1 presents an overview of the sampling, isotope parameters ( $\delta_{\text{initial}}$ ,  $\delta_{\text{med}}$ ,  $\Delta\delta$ ) and median values of meteorological  
238 variables from individual events. Sampled events had a duration of 141 or fewer minutes. The T and Twd exhibited small  
239 differences among the events. In contrast, RR, RH, LCL, Zc, w, and BT varied considerably between events. The maximum  
240 recorded values for these parameters were 97 %, 489 m, 46 dBZ, 8 m s<sup>-1</sup> and -63 °C, respectively.

241 Isotope values varied among convective events, with a range of -11.0 ‰, -92.8 ‰ and +15.7 ‰ for median values of  $\delta^{18}\text{O}$ ,  
242  $\delta^2\text{H}$  and *d*-excess, respectively. The maximum differences between the  $\delta_{\text{initial}}$  and  $\delta_{\text{med}}$  for  $\delta^{18}\text{O}$ ,  $\delta^2\text{H}$ , and *d*-excess were 1.6 ‰,  
243 9.1 ‰, and 9.5 ‰, respectively. The maximum  $\Delta\delta$  values for all isotopes parameters,  $\delta^{18}\text{O}$ ,  $\delta^2\text{H}$  and *d*-excess were 7.3 ‰, 43.0  
244 ‰ and 19.2 ‰, respectively.

### 245 3.2. Inter-event variability of the isotope parameters

246 Hysplit air mass back-trajectories revealed three main locations as moisture origin during the presence of convective rainfall:  
247 Amazon forest, Atlantic Ocean, and southern Brazil (Fig. 3). The sourcing of moisture for rainfall over Rio Claro varies



248 seasonally and spatially, suggesting complex interactions in moisture transport and mixing that strongly influence the initial  
249 isotopic composition of rainfall throughout the year (Table 1).

250 Summer rainfall events were characterized by the trajectory and length of moist air masses arriving from the Amazon forest  
251 (2020/02/10, 2020/02/01, and 2020/01/30) (Fig. 3a). As a result, there was a large amount of rainfall along Hysplit trajectories.  
252 Rainfall amounts were 177 mm, 126 mm and 78 mm, respectively, for these dates. Remarkably, these events exhibited very  
253 similar isotope characteristics ( $\delta^2\text{H}_{\text{initial}}$ ,  $\delta^{18}\text{O}_{\text{initial}}$ ) (Table 1). In contrast, the event on 2021/02/24 presented higher  $\delta_{\text{initial}}$  values,  
254 reflecting the oceanic moisture influence (Fig. 3a), with a lowest amount of rainfall (53 mm) along Hysplit trajectory.

255 Based on ERA-5, the vertically integrated eastward vapor flux corroborates the influence of a distinct mechanism for  
256 moisture transport and  $\delta_{\text{initial}}$  values. Negative values for vertical vapor fluxes over the Amazon forest during sampled  
257 convective events in summer (Fig. 4a, b, d) clearly illustrate a westward moisture flux from the Atlantic Ocean to the Amazon  
258 forest. Positive values in the central-southern region of Brazil indicate moisture being transported eastward from the Amazon  
259 forest. However, these moisture fluxes were not observed on 2021/02/24 when the eastward vapor flux was positive with high  
260 values over the Atlantic Ocean ( $250 \sim 750 \text{ kg m}^{-1} \text{ s}^{-1}$ ).

261 The autumn convective events on 2020/05/23 and 2020/06/09 revealed a significant continental origin of moist air masses  
262 (from south-western Brazil). In addition, during the second event, the Amazon-type trajectory started in the southern Atlantic  
263 and did not reach the boundary of the rainforest (Fig. 3b). In both autumn events, there was the lowest amount of rainfall (4  
264 mm) along Hysplit trajectories. On 2020/05/23 negative vertical flux values ( $-500 \sim -250 \text{ kg m}^{-1} \text{ s}^{-1}$ ) were observed in south-  
265 western Brazil, indicating moisture transport from the Atlantic Ocean to the continent. This favored a vapor flux ( $500 \sim 750$   
266  $\text{kg m}^{-1} \text{ s}^{-1}$ ) from western Brazil to the study area (Figure 4f). On 2020/06/09, there were slightly negative values ( $-250 \sim 0 \text{ kg}$   
267  $\text{m}^{-1} \text{ s}^{-1}$ ) of eastward vapor flux in the Amazon forest, indicating less influence from rainforest moisture. Conversely, positive  
268 vapor flux values ( $250 \sim 500 \text{ kg m}^{-1} \text{ s}^{-1}$ ) were observed in the western part of continental Brazil.

269 Two events in the spring season (Fig. 3c) also showed contrasting origin of moisture and initial  $d$ -excess values, despite  
270 only slight differences in  $\delta^{18}\text{O}_{\text{initial}}$  (Table 1). The mean trajectory on 2020/11/18 clearly belongs to the Amazon category,  
271 although it only passed over the south-eastern boundary of the Amazon rainforest and had a much shorter length and lower  
272 rainfall along Hysplit trajectory (23 mm) compared to the Amazon trajectories observed during the summer season. Thus,  
273 positive values of the eastward vapor flux ( $250 \sim 750 \text{ kg m}^{-1} \text{ s}^{-1}$ ) were not distributed along the Amazon forest to the Atlantic  
274 Ocean as typically observed (Fig. 4h). The mean trajectory on 2019/11/05 the eastward vapor flux ( $> 500 \text{ kg m}^{-1} \text{ s}^{-1}$ , Fig. 4g)  
275 were circling around Rio Claro, indicating the continental moisture origin (from southern Brazil), and low amount of rainfall  
276 along Hysplit trajectory of 8 mm.

### 277 3.3 Intra-event variability of the isotope and meteorological parameters

278 The temporal evolution of isotope characteristics and selected meteorological parameters of convective rainfall are shown in  
279 Fig. 5 (summer) and Fig. 6 (autumn-spring). The study emphasizes the lack of pattern in the measured values for reflectivity  
280 ( $Z_c$ ) in the vertical profile. Only higher  $Z_c$  values were observed near the surface (from 2km to 200m), which indicates an  
281 increase in rain rates. Despite the similar vertical structure, the temporal evolution varied considerably among events.  
282 Furthermore, the GOES-16 BT shows unique temporal patterns among events.

283 The differences in  $\Delta\delta$  observed between convective events were explained by intra-events (refer to Table 1) and how local  
284 factors may affect the regional isotopic signature as illustrated by the inter-event analysis.

### 285 3.3.1. Summer intra-events

286 Lower values of  $\Delta\delta^{18}\text{O}$  were observed on the 2020/02/01 and 2020/01/30 compared to higher  $\Delta\delta^{18}\text{O}$  values observed on the  
287 2020/02/10 and 2021/02/24. In contrast, all summer events exhibit high  $\Delta\delta$  values for  $d$ -excess (Table 1). Despite this variation  
288 in isotopic amplitude, the evolution of these events is characterized by different amounts of available humidity (Table 1 and  
289 Table 2). For the 2021/02/24 event, lower humidity values were observed below the cloud ( $\text{RH}_{\text{INT}} = 93\%$ ) and at the surface  
290 ( $\text{RH} 78 \sim 88\%$ , median value  $86\%$ ). The other events had higher humidity conditions ( $\text{RH}_{\text{INT}} = > 96\%$  and  $\text{RH} > 90\%$ ).  
291 Nevertheless, only 2021/02/24 and 2020/02/10 show  $d$ -excess values lower than  $10\%$ , suggesting that the specific local factors  
292 can influence the variations in the isotopic composition of the precipitation, as shown below for each event.

293 Specifically, the events on 2020/02/01 (Fig. 5c,e) and 2020/01/30 (Fig. 5d,f) showed consistent  $\delta^{18}\text{O}$  trends ( $-11.6 \sim -10.0$   
294  $\%$  and  $-10.6 \sim -9.6\%$ , respectively). In contrast, these events showed an inverted V-shaped (from  $11.3 \sim 15.3\%$  to  $15.4 \sim$   
295  $7.0\%$ ) and V-shaped (from  $20.8 \sim 11.4\%$  to  $14.6 \sim 16.2\%$ ) patterns for  $d$ -excess, respectively. The patterns of rainfall  
296 intensity were similar for both events, with high rainfall amount at the beginning of event, decreasing over the time. In BT  
297 values, decreased ( $-50 \sim -65\text{ }^\circ\text{C}$ ) and constant variations ( $-52 \sim -53\text{ }^\circ\text{C}$ ) occurred on 2020/02/01 and 2020/01/30 events,  
298 respectively. The strong and significant ( $p < 0.0001$ ) correlations were observed between isotopic composition and MRR  
299 parameters for 2020/02/01:  $\delta^{18}\text{O}$ - $Z_c$  ( $r = -0.9$ ),  $\delta^{18}\text{O}$ - $w$  ( $r = -0.9$ ),  $d$ -excess- $Z_c$  ( $r = 0.9$ ) and  $d$ -excess- $w$  ( $r = 0.9$ ), while there  
300 were no correlations between isotopic composition and meteorological parameters for 2020/01/30.

301 On 2021/02/24 (Fig. 5i,k) and 2020/02/10 (Fig. 5j,l), notable fluctuations were observed in both the isotope and  
302 meteorological parameters. On 2021/02/24,  $\delta^{18}\text{O}$  varied from  $-7.9 \sim -4.4\%$ , and  $d$ -excess varied from  $1.2$  to  $18.4\%$ . The  
303 evolution of the event was characterized by varying local weather conditions, as evidenced by a larger BT range ( $-38 \sim -57$   
304  $^\circ\text{C}$ ). Radar reflectivity is displayed in a vertical profile, illustrating these changes, with larger  $Z_c$  values during the event (red  
305 colors in Fig. 5g). As a result, three peaks of maximum rainfall amount were observed, which corresponded to the distinct  
306  $\delta^{18}\text{O}$  and for  $d$ -excess values: at 15:49 local time ( $2.6\text{ mm}$ ,  $-7.6\%$  and  $13.0\%$ ), at 16:24 ( $3.1\text{ mm}$ ,  $-6.9\%$  and  $8.4\%$ ) and at  
307 17:28 ( $3.3\text{ mm}$ ,  $-7.9\%$  and  $17.9\%$ ), respectively. Also, strong, and significant ( $p < 0.05$ ) correlation was observed between  
308  $\delta^{18}\text{O}$ - $R$  ( $r = -0.8$ ),  $d$ -excess- $R$  ( $r = -0.6$ ) and MRR parameter,  $\delta^{18}\text{O}$ - $Z_c$  ( $r = -0.6$ ) and  $d$ -excess- $Z_c$  ( $r = -0.5$ ).

309 On 2020/02/10,  $\delta^{18}\text{O}$  showed a variation from  $-15.2 \sim -7.9 \text{ ‰}$  and for  $d$ -excess from  $4.8 \sim 21.4 \text{ ‰}$ . During the beginning  
310 of the event and until 21:03 local time, high BT values ( $-16 \sim -45 \text{ °C}$ ) corresponded to the higher Zc values (red colors in Fig.  
311 5h) and high RH ( $\sim 97 \text{ ‰}$ ). After this time, lower Zc and lowest BT values were observed ( $-45 \sim -57 \text{ °C}$ ). There were two  
312 breakpoints in the rainfall trend (increasing to decreasing) corresponding to the change in isotope values ( $\delta^{18}\text{O}$  and  $d$ -excess),  
313 occurring at 20:36 ( $4.8$  to  $3.2 \text{ mm}$ ,  $-13.9$  to  $-9.5 \text{ ‰}$  and  $15.7$  to  $9.4 \text{ ‰}$ ) and 21:57 ( $2.0$  to  $0.8 \text{ mm}$ ,  $-14.9$  to  $-7.9 \text{ ‰}$  and  $21.4$  to  
314  $4.8 \text{ ‰}$ ) respectively. In addition, for this event strong and significant ( $p < 0.05$ ) correlation was observed only between  $\delta^{18}\text{O}$ -  
315 RH ( $r = -0.5$ ) and  $d$ -excess-RH ( $r = 0.5$ ).

### 316 3.3.2 Autumn and spring intra-events

317 Lower  $\Delta\delta^{18}\text{O}$  values were observed during autumn and spring events in comparison to summer events. Both autumn and spring  
318 events showed higher  $\Delta\delta$  values for  $d$ -excess when compared to summer events. For the events on 2020/05/23 ( $\text{RH}_{\text{INT}} = 93 \text{ ‰}$ ,  
319 RH  $78 \sim 89 \text{ ‰}$ , with median of  $87 \text{ ‰}$ ) and 2020/11/18 ( $\text{RH}_{\text{INT}} = 92 \text{ ‰}$  and RH  $70 \sim 90 \text{ ‰}$ , with median of  $85 \text{ ‰}$ ), lower humidity  
320 conditions were recorded, whereas for all other events, humidity conditions were high ( $\text{RH}_{\text{INT}} = > 97 \text{ ‰}$  and RH  $= > 90 \text{ ‰}$ ) as  
321 show in Tables 1 and 2.

322 For autumn events on 2020/06/09 (Fig. 6a,c,e) and 2020/05/23 (Fig. 6b,d,f), a slight increase trend ( $-3.7 \sim -1.5 \text{ ‰}$ ) and  
323 stationary trend ( $-2.6 \sim -2.7 \text{ ‰}$ ) were observed regarding  $\delta^{18}\text{O}$ . On the other hand, for the same events,  $d$ -excess showed a W-  
324 shaped trend ( $17.7 \sim 6.3 \text{ ‰}$ , during the last part of the event) and V-shaped pattern ( $16.7 \sim 19.0 \text{ ‰}$ ), respectively. Both events  
325 demonstrated a decrease in rainfall amount: from  $6.2$  to  $0.2 \text{ mm}$  on 2020/06/09, 2020, and from  $2.6$  to  $0.2 \text{ mm}$  on 2020/05/23.  
326 Additionally, the range of BT increased from  $-55 \text{ °C}$  to  $-35 \text{ °C}$  and from  $-60 \text{ °C}$  to  $-52 \text{ °C}$ , respectively. Strong and significant  
327 ( $p < 0.05$ ) correlations were observed between isotopic and surface meteorological parameters during the event on 2020/06/09,  
328  $\delta^{18}\text{O}$ -RH ( $r = 0.5$ ),  $\delta^{18}\text{O}$ -T ( $r = -0.6$ ),  $d$ -excess-RH ( $r = -0.6$ ), and  $d$ -excess-T ( $r = 0.7$ ). However, no significant correlations  
329 were found during the event on 2020/05/23.

330 Spring convective events exhibited contrasting variations in isotopes and meteorological conditions. On 2019/11/05 (Fig.  
331 6g,i,k), slight fluctuations were observed in  $\delta^{18}\text{O}$  ( $-3.0 \sim -1.7 \text{ ‰}$ , slightly increasing-trend), while  $d$ -excess values were higher  
332 ( $21.0 \sim 28.0 \text{ ‰}$ , decreasing trend). This slight fluctuations in  $\delta^{18}\text{O}$  values correspond to the constant and higher Zc near surface.  
333 This is evidenced by the highest and significant ( $p < 0.0003$ ) correlations observed between isotopic and MRR parameters,  
334  $\delta^{18}\text{O}$ -Zc ( $r = -0.7$ ),  $\delta^{18}\text{O}$ -w ( $r = -0.7$ ), and  $d$ -excess-w ( $r = 0.6$ ). In contrast, these fluctuations were not related with changes in  
335 rainfall amount ( $0.6 \sim 5.0 \text{ mm}$ ) and BT ( $-65 \sim -62 \text{ °C}$ ).

336 On 2020/11/18, two distinct steps revealed a decreasing trend in  $\delta^{18}\text{O}$  ( $-2.7 \sim -5.4 \text{ ‰}$ ), and a substantial increasing trend in  
337  $d$ -excess ( $10.2 \sim 23.1 \text{ ‰}$ ) (Fig. 6h,j,l). Between 15:10 and 16:05 local time, the vertical profile of the MRR exhibited variable  
338 Zc values, with concomitant decreases in both BT values ( $-62$  and  $-65 \text{ °C}$ ) and  $\delta^{18}\text{O}$  ( $-2.7 \sim -4.0 \text{ ‰}$ ) and increase in both rainfall  
339 ( $1.2 \sim 2.0 \text{ mm}$ ),  $d$ -excess ( $10.2 \sim 19.6 \text{ ‰}$ ) and RH ( $70 \sim 82 \text{ ‰}$ ) values. After this period, Zc values increased closer to the

340 surface, resulting in a slight decrease in temperature ( $-65 \sim -63$  °C). Additionally,  $\delta^{18}\text{O}$ ,  $d$ -excess, rainfall amount and RH  
341 fluctuated ( $-3.8 \sim -5.4$  ‰,  $18.0 \sim 23.1$  ‰,  $1.8 \sim 2.2$  mm and  $84 \sim 90$  %, respectively). Regardless of this, no significant  
342 correlations were found due to the considerable variations between isotopic and rainfall, as well as BT and MRR parameters.  
343 The significant ( $p < 0.001$ ) correlations were only observed for  $\delta^{18}\text{O}$ -RH ( $r = -0.9$ ),  $\delta^{18}\text{O}$ -T ( $r = 0.9$ ),  $d$ -excess-RH ( $r = 0.9$ ),  
344 and  $d$ -excess-T ( $r = -0.9$ ).

## 345 **4. Discussion**

346 Detailed evaluations of isotopic variability in convective rainfall were provided by both inter- and intra-events. Such separation  
347 between inter- and intra-events allows for improved evaluation of fractionation processes that occurred during moisture  
348 transport towards the formation of local rainfall. Generally, during the summer, thermal conditions dominate convective  
349 processes, while during autumn and spring, convective rainfall is associated with frontal systems (Fig. 2). It is crucial to  
350 quantify these synoptic variations to understand seasonal differences in atmospheric conditions, which affect moisture source  
351 and transport across seasons. Thus, the  $\delta_{\text{initial}}$  values are influenced by vapor origin, convective activity, and weather systems,  
352 which may be further modified by local processes, resulting in distinct values of  $\delta_{\text{med}}$  and large  $\Delta\delta$ .

353 The key regional and local controls of the isotopic composition of convective rainfall are, respectively: (i) rainfall of moist  
354 air masses during their transport in the atmosphere, from the source region(s) to the collection site showed by inter-event  
355 analysis, and (ii) local effects associated with convective cloud characteristics, vertical rainfall structure and near-surface  
356 humidity conditions.

### 357 **4.1 Regional atmospheric controls**

358 Regional aspects of atmospheric moisture transport to the Rio Claro site were illustrated in HYSPLIT backward trajectories  
359 (Fig. 3) and maps of vertically integrated moisture flux in the region (Fig. 4). Most of moist air masses arriving at Rio Claro  
360 during summer (2020/02/10, 2020/02/01, and 2020/01/30) exhibited a common origin in the equatorial Atlantic Ocean and  
361 were subjected to a long rainfall of moist air masses, extending over several thousand kilometers. Along this pathway, air  
362 masses interacted with the Amazon forest. Intensive recycling of moisture leads to a small continental gradient of  $\delta$ -values of  
363 rainfall across the Amazon forest (Salati et al., 1979; Rozanski et al., 1993) and elevated  $d$ -excess (Gat, J. R., & Matsui, 1991).  
364 At Rio Claro, the arriving air masses are depleted in heavy isotopes ( $\delta_{\text{initial}} \leq -10.0$  ‰) due to enhanced amount of rainfall along  
365 the trajectories ( $\geq 78$  mm), after the southeastern deflection from the Andes, with consistent initial  $d$ -excess higher than  $+10.0$   
366 ‰, inherited through the interaction of maritime moisture with the Amazon forest. In contrast, the summer event on 2021/02/24  
367 was influenced by oceanic moisture and had a short trajectory compared to the other summer events, as indicated by the lower

368 amount of rainfall along the Hysplit trajectory (53 mm), which explains the higher  $\delta_{\text{initial}}^{18\text{O}}$  values ( $\delta^{18\text{O}} = -7.6 \text{ ‰}$  and  $d\text{-excess}$   
369  $= +13 \text{ ‰}$ ).

370 The convective events representing spring and autumn season exhibited substantially shorter trajectories suggesting that  
371 the atmospheric “pump” transporting moisture from the equatorial Atlantic Ocean to the Amazon forest was much weaker or  
372 non-existent during this time of the year. As a result, those trajectories were characterized by a reduction in the amount of  
373 rainfall along the trajectories and enriched  $\delta_{\text{initial}}^{18\text{O}}$  ( $\geq -3.1 \text{ ‰}$ ) and higher initial  $d\text{-excess}$  ( $\geq +10.0 \text{ ‰}$ ).

374 In addition, the highest initial  $d\text{-excess}$  ( $\geq 24.1 \text{ ‰}$ ) were observed on 2019/11/05 and 2020/09/06 events. A possible  
375 explanation of these greater  $d\text{-excess}$  values may be enhanced interaction with the surface of the continent, resulting in  
376 evapotranspiration processes. At steady state, transpiration is a non-fractionating process. This means that soil water pumped  
377 by plants returns to the atmosphere without any detectable change in its isotopic composition (Cuntz et al., 2007; Flanagan et  
378 al., 1991; Dongmann and Nürnberg, 1974). If it is assumed that soil water available to plants has isotopic characteristics equal  
379 to the mean values of the two events described, then the water vapor released to the local atmosphere during transpiration will  
380 possess identical isotopic signatures. Now, assuming that this water vapor is lifted by convection and then condenses, it is  
381 possible to easily calculate the isotopic composition of the first condensate. Assuming an isotopic equilibrium between the  
382 gaseous and liquid phases of water in the cloud:

$$383 \delta_L = \alpha_{eq}(1000 + \delta_V) - 1000 \quad (7)$$

384 where  $\delta_L$  and  $\delta_V$  signify delta values of liquid (condensate) and vapor phase, respectively, at isotopic equilibrium, whereas  $\alpha_{eq}$   
385 stands for equilibrium fractionation factor. Equilibrium fractionation factors for  $^2\text{H}$ ,  $^{18}\text{O}$  and  $d\text{-excess}$  were calculated using  
386 empirical expressions proposed by (Horita and Wesolowski, 1994). The assumed condensation temperature was equal  $20 \text{ °C}$   
387 and  $18 \text{ °C}$  (cf. Tdw for 2019/11/05 and 2020/06/09, respectively in Table 1). The calculated isotopic characteristics of the first  
388 condensate are equal  $\delta^2\text{H} = +85.1 \text{ ‰}$ ,  $\delta^{18}\text{O} = +6.6 \text{ ‰}$ ,  $d\text{-excess} = +32.3 \text{ ‰}$  and  $\delta^2\text{H} = +81.0 \text{ ‰}$ ,  $\delta^{18}\text{O} = +6.5 \text{ ‰}$ ,  $d\text{-excess} =$   
389  $+28.8 \text{ ‰}$ , for both respectively events. This example calculation suggests the transpiration process could generate isotopically  
390 enriched rainfall and greater  $d\text{-excess}$ .

391 Thus, these regional processes were imprinted in the initial isotopic composition ( $\delta^{18}\text{O}_{\text{initial}}$  and  $d\text{-excess}$ ) of all convective  
392 events. This regional  $\delta$ -signature was preserved during summer (2020/01/30 and 2020/02/01), autumn (2020/06/09) and spring  
393 (2019/11/05) events, as indicated by similar  $\delta^{18}\text{O}_{\text{initial}}$ ,  $\delta^{18}\text{O}_{\text{med}}$ , lower  $\Delta\delta^{18}\text{O}$  values. In addition, the  $d\text{-excess}$  exhibited greater  
394 difference between  $\delta_{\text{initial}}$  and  $\delta_{\text{med}}$ , and higher  $\delta\Delta$  values in relation to the  $\delta^{18}\text{O}$  parameters for all convective rainfall events.  
395 The following section provides more detail on the variability of  $d\text{-excess}$  in terms of local atmospheric processes.

## 396 4.2 Local atmospheric controls

397 The events on summer (2020/02/10 and 2021/02/24), autumn (2020/05/23) and spring (2020/11/18) exhibited substantial  
398 differences in  $\delta_{\text{initial}}$ ,  $\delta_{\text{med}}$ , and higher  $\Delta\delta$  for  $\delta^{18}\text{O}$ ,  $\delta^2\text{H}$  and  $d$ -excess (Table 1), implying that local processes modified the  
399 regional isotopic imprint.

400 Overall, the Rayleigh distillation governs the depletion of isotopic composition for the events 2020/02/10 ( $^{18}\text{O}_{\text{initial}} = -12.3$   
401 ‰ and  $\delta^{18}\text{O}_{\text{med}} = -13.9$  ‰) and 2020/11/18 ( $^{18}\text{O}_{\text{initial}} = -2.7$  ‰ and  $\delta^{18}\text{O}_{\text{med}} = -4.1$  ‰). This depletion is linked to a reduction of  
402 isotopic exchange and the local increase in cloud-top heights, which leads to a rise in BT values observed at both events,  
403 ranging from -16 to -45 °C (Fig. 5l) and -62 and -65 °C (Fig. 6l), respectively. The intra-event analysis facilitates identification  
404 of variable fractionation processes during the evolution of these rainfall systems. The  $\delta^{18}\text{O}$  trends of both events show  
405 similarities, but notable differences in  $d$ -excess trends occur due to varying vertical profiles and RH conditions. On 2020/02/10,  
406 the Zc changed towards the end of the event while RH remained consistently high (97 %). This induced a change in  $d$ -excess  
407 during a specific time of the event. On the other hand, on 2020/11/18, Zc was varied at the beginning of event with lower RH  
408 of 70 ~ 82 %, leading to a lower  $d$ -excess during the start of event. The observed strong and significant correlations between  
409 isotopic composition and RH support this variation for both events.

410 The event of 2021/02/24 provides a suitable example of the impact of local factors. The marked differences between the  
411 initial and median values for  $d$ -excess (13 ‰ and 7.2 ‰, respectively) and the isotopic composition, enriched with initial  
412 ( $\delta^{18}\text{O}_{\text{initial}} = -7.6$  ‰ and  $\delta^2\text{H}_{\text{initial}} = -47.8$  ‰) and median ( $\delta^{18}\text{O}_{\text{med}} = -6.8$  ‰ and  $\delta^2\text{H}_{\text{med}} = -44.8$  ‰) values (Table 1), resulted in a  
413 distinctive enrichment in the isotopic composition. This enrichment is associated with the diverse vertical structure of rainfall  
414 and low humidity conditions (RH, 78 ~ 88%). Alterations in both rainfall patterns and Zc levels under low humidity conditions  
415 promote the preferential escape of lighter isotopologues from liquid water (Dansgaard, 1964). This is corroborated by notable  
416 and negative correlations between isotopic composition, rainfall volume, and Zc. In addition, the preferential escape of lighter  
417 isotopologues also occurred during the 2020/05/23, characterized by lower RH (78 ~ 89 %), resulted in enriched isotopic  
418 composition.

419 The semi-quantitative evaluation illustrated in Table 2 reinforces the intra-event analysis, suggesting a modification of the  
420 mean  $d$ -excess. The intra-event results indicate that local changes in the isotopic composition of rainfall are controlled by the  
421 specific cloud characteristics and the vertical structure of rainfall, which are connected to local humidity conditions. Therefore,  
422 the reduction in  $d$ -excess was greater during the events on 2021/02/24, 2020/05/23, and 2020/11/18 due to cloud features and  
423 low humidity conditions, compared to the event on 2020/02/10 that had high local humidity conditions.

## 424 **5 Concluding remarks**

425 The study employed high-frequency isotope parameters ( $\delta_{\text{initial}}$ ,  $\delta_{\text{med}}$ , and  $\Delta\delta$ ) as well as meteorological data to investigate  
426 the regional and local mechanisms controlling the isotopic characteristics of convective precipitation.

427 Based on inter-event analysis, it has been revealed that the regional isotopic characteristics are different between summer  
428 and autumn-spring seasons. The  $\delta_{\text{initial}}$  is determined by moisture transport mechanisms and convection features. The key  
429 factors are progressive rainfall along trajectories and Rayleigh distillation along the moisture transport pathway. The effect of  
430 rainfall along trajectories is pronounced during summer events, associated with the longer moisture transport pathway from  
431 the Amazon forest, which produces depleted heavy isotopes. In contrast, reduced autumn and spring rainfall along trajectories  
432 are associated with the shorter moisture transport pathway from the Atlantic Ocean and southern Brazil, producing enriched  
433 isotope characteristics. This regional  $\delta$ -signature has been preserved in both summer, autumn, and spring events. Specific  
434 events in autumn and spring with high  $d$ -excess values were associated with evapotranspiration processes along the moisture  
435 transport pathway, demonstrating how regional convective processes interact with the tropical surface and alter the isotopic  
436 composition.

437 During the advance of convective rainfall, the regional  $\delta$ -signature was altered by local effects generated the isotope  
438 variability (large  $\Delta\delta$  values), as shown by the intra-event evaluation. The critical local controls are the cloud changes and the  
439 vertical structure of the rainfall. The local controls occur under certain specific conditions of low relative humidity of ambient.  
440 These local mechanisms amplify the discrepancy between the  $\delta_{\text{initial}}$  and  $\delta_{\text{med}}$  values, leading to significant  $\Delta\delta$  values.  
441 Significant correlations between  $\delta^{18}\text{O}$ ,  $d$ -excess,  $Z_c$ , and RH, as well as the semi-quantitative evaluation, lend support to the  
442 significance of the vertical structure and relative humidity conditions outlined in this study.

443 Therefore, the convective rainfall is controlled by an interplay of regional and local factors. The complex and dynamic  
444 conditions of convective rainfall formation across the tropics can be understood using high-frequency analysis. Through  
445 identifying the complexity of the factors that make up the isotopic composition of convective rainfall in the study area, it was  
446 possible to understand why it was so difficult to apply regression models in past studies when using daily data and separation  
447 of rainfall types for the Rio Claro GNIP station.

448 Although high-frequency rainfall sampling is logistically difficult, we encourage future studies of this type in different  
449 geographical regions across the tropics, to better understand the factors controlling the isotopic composition of convective  
450 rainfall during rainy period. Extensive monitoring of local meteorological parameters and modeling of regional moisture  
451 transport to the rainfall collection site, along with the application of more robust below-cloud models, should accompany such  
452 studies.

#### 453 **Data availability**

454 A complete database (isotope characteristics of rainfall as well as selected meteorological parameters characterizing these  
455 events) are available at: <https://doi.org/10.17632/kk3gs8zn4s.1> (dos Santos et al., 2023). Monthly GNIP data:  
456 <https://www.iaea.org/services/networks/gnip>. GOES-16 imageries are available at:  
457 [https://home.chpc.utah.edu/~u0553130/Brian\\_Blalock/cgi-bin/goes16\\_download.cgi](https://home.chpc.utah.edu/~u0553130/Brian_Blalock/cgi-bin/goes16_download.cgi). The weather systems are available at:  
458 <https://www.marinha.mil.br/chm/dados-do-smm-cartas-sinoticas/cartas-sinoticas> and

459 <http://tempo.cptec.inpe.br/boletimtecnico/pt>. Reanalysis data are available at:  
460 (<https://cds.climate.copernicus.eu/cdsapp#!/search?type=dataset>. The Global Modeling and Assimilation Office (GMAO) data  
461 are available at: <https://goldsmr4.gesdisc.eosdis.nasa.gov/data/MERRA2/M2T1NXFLX.5.12.4/>).

462 Goddard Earth Sciences Data and Information Services Center (GES DISC) data are available at:  
463 [https://disc.gsfc.nasa.gov/datasets/AIRS3STD\\_7.0/summary](https://disc.gsfc.nasa.gov/datasets/AIRS3STD_7.0/summary).

464

#### 465 *Acknowledgment*

466 FAPESP support for the scholarship provided under the Process 2019/03467-3 and 2021/10538-4 is acknowledged. Durán-  
467 Quesada acknowledges time for analysis and writing provided within UCR C1038 project. The authors acknowledge Troy G.  
468 for English revision.

469

#### 470 **Financial support**

471 This work was funded by grants the São Paulo Research Foundation (FAPESP) under Processes 2018/06666-4, 2019/03467-  
472 3 and 2021/10538-4, and by the International Atomic Energy Agency Grant CRP-F31006.

#### 473 **References**

474 Adler, R. F. and Fenn, D. D.: Thunderstorm vertical velocities estimated from satellite data, *American*, 36, 1747–1754,  
475 [https://doi.org/10.1175/1520-0469\(1979\)036,1747:TVVEFS.2.0.CO;2](https://doi.org/10.1175/1520-0469(1979)036,1747:TVVEFS.2.0.CO;2), 1979.

476 Adler, R. F. and Mack, R. A.: Thunderstorm cloud top dynamics as inferred from satellite observations and a cloud top parcel  
477 model, *American Meteorological Society*, 43, 1945–1960, [https://doi.org/10.1175/1520-0469\(1986\)043,1945:TCTDAI.2.0.CO;2](https://doi.org/10.1175/1520-0469(1986)043,1945:TCTDAI.2.0.CO;2), 1986.

479 Aemisegger, F. ., Spiegel, J. K. ., Pfahl, S. ., Sodemann, H. ., Eugster, W. ., and Wernli, H.: Isotope meteorology of cold front  
480 passages: A case study combining observations and modeling, *Geophysical Research Letters*, 42, 5652–5660,  
481 <https://doi.org/10.1002/2015GL063988>, 2015.

482 Aggarwal, P. K., Romatschke, U., Araguas-Araguas, L., Belachew, D., Longstaffe, F. J., Berg, P., Schumacher, C., and Funk,  
483 A.: Proportions of convective and stratiform precipitation revealed in water isotope ratios, *Nature Geoscience*, 9, 624–629,  
484 <https://doi.org/10.1038/ngeo2739>, 2016.

485 Bony, S., Risi, C., and Vimeux, F.: Influence of convective processes on the isotopic composition ( $\delta^{18}\text{O}$  and  $\delta\text{D}$ ) of  
486 precipitation and water vapor in the tropics: 1. Radiative-convective equilibrium and Tropical Ocean–Global Atmosphere–  
487 Coupled Ocean-Atmosphere Response Experiment (TOGA-CO), *Journal of Geophysical Research: Atmospheres*, 113, 1–21,  
488 <https://doi.org/10.1029/2008JD009942>, 2008.

489 Breugem, A. J., Wesseling, J. G., Oostindie, K., and Ritsema, C. J.: Meteorological aspects of heavy precipitation in relation  
490 to floods – An overview, *Earth-Science Reviews*, 204, 103171, <https://doi.org/10.1016/j.earscirev.2020.103171>, 2020.



491 Cecchini, M. A., Machado, L. A. T., and Artaxo, P.: Droplet Size Distributions as a function of rainy system type and Cloud  
492 Condensation Nuclei concentrations, *Atmospheric Research*, 143, 301–312, <https://doi.org/10.1016/j.atmosres.2014.02.022>,  
493 2014.

494 Celle-Jeanton, H., Gonfiantini, R., Travi, Y., and Sol, B.: Oxygen-18 variations of rainwater during precipitation: Application  
495 of the Rayleigh model to selected rainfalls in Southern France, *Journal of Hydrology*, 289, 165–177,  
496 <https://doi.org/10.1016/j.jhydrol.2003.11.017>, 2004.

497 Coplen, T. B., Neiman, P. J., White, A. B., Landwehr, J. M., Ralph, F. M., and Dettinger, M. D.: Extreme changes in stable  
498 hydrogen isotopes and precipitation characteristics in a landfalling Pacific storm, *Geophysical Research Letters*, 35, L21808,  
499 <https://doi.org/10.1029/2008GL035481>, 2008.

500 Craig, H. and Gordon, L. I.: Deuterium and oxygen-18 variations in the ocean and the marine atmosphere., edited by:  
501 Tongiorgi, E., *Stable isotopes in oceanographic and paleotemperatures*, Pisa, 9–130 pp., 1965.

502 Cuntz, M., Ogée, J., Farquhar, G. D., Peylin, P., and Cernusak, L. A.: Modelling advection and diffusion of water isotopologues  
503 in leaves, *Plant, Cell and Environment*, 30, 892–909, <https://doi.org/10.1111/j.1365-3040.2007.01676.x>, 2007.

504 Dansgaard, W.: Stable isotopes in precipitation, *Tellus*, 16, 436–468, <https://doi.org/10.3402/tellusa.v16i4.8993>, 1964.

505 Donat, M. G., Alexander, L. V., Yang, H., Durre, I., Vose, R., Dunn, R. J. H., Willett, K. M., Aguilar, E., Brunet, M., Caesar,  
506 J., Hewitson, B., Jack, C., Klein Tank, A. M. G., Kruger, A. C., Marengo, J., Peterson, T. C., Renom, M., Oria Rojas, C.,  
507 Rusticucci, M., Salinger, J., Elayah, A. S., Sekele, S. S., Srivastava, A. K., Trewin, B., Villarroel, C., Vincent, L. A., Zhai, P.,  
508 Zhang, X., and Kitching, S.: Updated analyses of temperature and precipitation extreme indices since the beginning of the  
509 twentieth century: The HadEX2 dataset, *Journal of Geophysical Research Atmospheres*, 118, 2098–2118,  
510 <https://doi.org/10.1002/jgrd.50150>, 2013.

511 Dongmann, G. and Nürnberg, H. W.: On the Enrichment of H<sub>2</sub>18O in the Leaves of Transpiring Plants, *Radiation and*  
512 *Environmental Biophysics*, 52, 41–52, 1974.

513 Endries, J. L., Perry, L. B., Yuter, S. E., Seimon, A., Andrade-Flores, M., Winkelmann, R., Quispe, N., Rado, M., Montoya,  
514 N., Velarde, F., and Arias, S.: Radar-observed characteristics of precipitation in the tropical high andes of Southern Peru and  
515 Bolivia, *Journal of Applied Meteorology and Climatology*, 57, 1441–1458, <https://doi.org/10.1175/JAMC-D-17-0248.1>, 2018.

516 van der Ent, R. J. and Tuinenburg, O. A.: The residence time of water in the atmosphere revisited, *Hydrology and Earth System*  
517 *Sciences*, 21, 779–790, <https://doi.org/10.5194/hess-21-779-2017>, 2017.

518 Flanagan, L. B., Comstock, J. P., and Ehleringer, J. R.: Comparison of modeled and observed environmental influences on the  
519 stable oxygen and hydrogen isotope composition of leaf water in *Phaseolus vulgaris* L, *Plant Physiology*, 96, 588–596,  
520 <https://doi.org/10.1104/pp.96.2.588>, 1991.

521 Froehlich, K., Gibson, J. J., and Aggarwal, P.: Deuterium excess in precipitation and its climatological significance, *Journal*  
522 *of Geophysical Research-Atmospheres*, 1–23, 2002.

523 Gadgil, S.: The Indian monsoon and its variability, *Annual Review of Earth and Planetary Sciences*, 31, 429–467,  
524 <https://doi.org/10.1146/annurev.earth.31.100901.141251>, 2003.

525 Galewsky, J., Schneider, M., Diekmann, C., Semie, A., Bony, S., Risi, C., Emanuel, K., and Brogniez, H.: The Influence of  
526 Convective Aggregation on the Stable Isotopic Composition of Water Vapor, *AGU Advances*, 4, 1–16,  
527 <https://doi.org/10.1029/2023AV000877>, 2023.

528 García-Santos, S., Sánchez-Murillo, R., Peña-Paz, T., Chirinos-Escobar, M. J., Hernández-Ortiz, J. O., Mejía-Escobar, E. J.,  
529 and Ortega, L.: Water stable isotopes reveal a complex rainfall to groundwater connectivity in central Honduras, *Science of*  
530 *the Total Environment*, 844, <https://doi.org/10.1016/j.scitotenv.2022.156941>, 2022.

531 Garreaud, R. D.: Cold air incursions over subtropical South America: Mean structure and dynamics, *Monthly Weather Review*,  
532 128, 2544–2559, [https://doi.org/10.1175/1520-0493\(2000\)128<2544:caioss>2.0.co;2](https://doi.org/10.1175/1520-0493(2000)128<2544:caioss>2.0.co;2), 2000.

533 Gat, J. R., & Matsui, E.: Atmospheric water balance in the Amazon Basin: An isotopic evapotranspiration model, *Journal of*  
534 *Geophysical Research*, 96, 13179–13188, <https://doi.org/https://doi.org/10.1029/91JD00054>, 1991.

535 Gat, J. R.: Environmental isotopes in the hydrological cycle: Principles and applications. Volume II, Atmospheric water,  
536 *Technical documents in hydrology*, Paris, 1–113 pp., 2001.

537 Gimeno, L., Drumond, A., Nieto, R., Trigo, R. M., and Stohl, A.: On the origin of continental precipitation, *Geophysical*  
538 *Research Letters*, 37, 1–7, <https://doi.org/10.1029/2010GL043712>, 2010.

539 Gimeno, L., Vázquez, M., Eiras-Barca, J., Sorí, R., Stojanovic, M., Algarra, I., Nieto, R., Ramos, A. M., Durán-Quesada, A.  
540 M., and Dominguez, F.: Recent progress on the sources of continental precipitation as revealed by moisture transport analysis,  
541 *Earth-Science Reviews*, 201, 103070, <https://doi.org/10.1016/j.earscirev.2019.103070>, 2020.

542 Gonfiantini, R.: Environmental isotopes in lake studies, in: *Handbook of Environmental Isotope Geochemistry Vol. 2 The*  
543 *Terrestrial Environment*, vol. 2, Elsevier, Amsterdam, 113–168, 1986.

544 Graf, P., Wernli, H., Pfahl, S., and Sodemann, H.: A new interpretative framework for below-cloud effects on stable water  
545 isotopes in vapour and rain, *Atmospheric Chemistry and Physics*, 19, 747–765, <https://doi.org/10.5194/acp-19-747-2019>,  
546 2019.

547 Han, X., Lang, Y., Wang, T., Liu, C.-Q., Li, F., Wang, F., Guo, Q., Li, S., Liu, M., Wang, Y., and Xu, A.: Temporal and spatial  
548 variations in stable isotopic compositions of precipitation during the typhoon Lekima (2019), China, *Science of The Total*  
549 *Environment*, 762, 143143, <https://doi.org/10.1016/j.scitotenv.2020.143143>, 2021.

550 He, S., Goodkin, N. F., Kurita, N., Wang, X., and Rubin, C. M.: Stable isotopes of Precipitation During Tropical Sumatra  
551 Squalls in Singapore, *Journal of Geophysical Research: Atmospheres*, 123, 3812–3829,  
552 <https://doi.org/10.1002/2017JD027829>, 2018.

553 Horita, J. and Wesolowski, D. J.: Horita and Wesolowski 1994, *Geochimica et Cosmochimica Acta*, 58, 1–13, 1994.

554 Horita, J., Rozanski, K., and Cohen, S.: Isotope effects in the evaporation of water: a status report of the Craig–Gordon model,  
555 *Isotopes in Environmental and Health Studies*, 44, 23–49, <https://doi.org/10.1080/10256010801887174>, 2008.

556 Houze, R.: Stratiform precipitation in regions of convection: A Meteorological Paradox?, *Bulletin of the American*  
557 *Meteorological Society*, 78, 2179–2195, 1997.

558 Houze, R. A.: *Cloud dynamics*, Academic Press Limited, 573 pp., [https://doi.org/10.1016/0377-0265\(87\)90017-0](https://doi.org/10.1016/0377-0265(87)90017-0), 1993.

559 Houze, R. A.: Mesoscale Convective Systems, in: *International Geophysics*, vol. 104, 237–286, <https://doi.org/10.1016/B978-0-12-374266-7.00009-3>, 2004.

561 Houze, R. A. J.: Observed structure of mesoscale convective systems and implications for large-scale heating., *Quart. J. Roy. Meteor. Soc.*, 115, 425–461, 1989.

563 IAEA: IAEA / GNIP precipitation sampling guide V2.02, *Global Network of Isotopes in Precipitation (GNIP)*, 20, 2014.

564 IPCC, W. G. I.-T. P. S. B.: Regional fact sheet – Central and South America, *Sixth Assessment Report*, 1–2 pp., 2021.

565 Jeelani, G., Deshpande, R. D., Galkowski, M., and Rozanski, K.: Isotopic composition of daily precipitation along the southern foothills of the Himalayas: Impact of marine and continental sources of atmospheric moisture, *Atmospheric Chemistry and Physics*, 18, 8789–8805, <https://doi.org/10.5194/acp-18-8789-2018>, 2018.

566  
567  
568 Kastman, J., Market, P., Fox, N., Foscatto, A., and Lupo, A.: Lightning and Rainfall Characteristics in Elevated vs. Surface Based Convection in the Midwest that Produce Heavy Rainfall, *Atmosphere*, 8, 36, <https://doi.org/10.3390/atmos8020036>, 2017.

571 Klaassen, W.: Radar Observations and Simulation of the Melting Layer of Precipitation, *Journal of the Atmospheric Sciences*, 45, 3741–3753, 1988.

573 Kodama, Y.: Large-scale common features of subtropical precipitation zones ( the Baiu Frontal Zone , the SPCZ , and the SACZ ) Part I: Characteristics of subtropical frontal zones, *Journal of the Meteorological Society of Japan*, 70, 813–836, <https://doi.org/10.1248/cpb.37.3229>, 1992.

574  
575  
576 Kurita, N.: Water isotopic variability in response to mesoscale convective system over the tropical ocean, *Journal of Geophysical Research Atmospheres*, 118, 10376–10390, <https://doi.org/10.1002/jgrd.50754>, 2013.

577  
578 Kurita, N., Ichiyanagi, K., Matsumoto, J., Yamanaka, M. D., and Ohata, T.: The relationship between the isotopic content of precipitation and the precipitation amount in tropical regions, *Journal of Geochemical Exploration*, 102, 113–122, <https://doi.org/10.1016/j.gexplo.2009.03.002>, 2009.

579  
580  
581 Lacour, J. L., Risi, C., Worden, J., Clerbaux, C., and Coheur, P. F.: Importance of depth and intensity of convection on the isotopic composition of water vapor as seen from IASI and TES  $\delta D$  observations, *Earth and Planetary Science Letters*, 481, 387–394, <https://doi.org/10.1016/j.epsl.2017.10.048>, 2018.

582  
583  
584 Lawrence, J. R., Gedzelman, S. D., Dexheimer, D., Cho, H., Carrie, G. D., Gasparini, R., Anderson, C. R., Bowman, K. P., and Biggerstaff, M. I.: Stable isotopic composition of water vapor in the tropics, *Journal of Geophysical Research: Atmospheres*, 109, 16, <https://doi.org/10.1029/2003JD004046>, 2004.

585  
586  
587 Lee, J. and Fung, I.: “Amount effect” of water isotopes and quantitative analysis of post-condensation processes, *Hydrological Processes*, 22, 1–8, <https://doi.org/10.1002/hyp.6637>, 2008.

588  
589 Lekshmy, P. R., Midhun, M., Ramesh, R., and Jani, R. A.:  $^{18}O$  depletion in monsoon rain relates to large scale organized convection rather than the amount of rainfall, *Scientific Reports*, 4, 1–5, <https://doi.org/10.1038/srep05661>, 2014.

590  
591 Lima, K. C., Satyamurty, P., and Fernández, J. P. R.: Large-scale atmospheric conditions associated with heavy rainfall episodes in Southeast Brazil, *Theoretical and Applied Climatology*, 101, 121–135, <https://doi.org/10.1007/s00704-009-0207->

592

593 9, 2010.

594 Luiz Silva, W., Xavier, L. N. R., Maceira, M. E. P., and Rotunno, O. C.: Climatological and hydrological patterns and verified  
595 trends in precipitation and streamflow in the basins of Brazilian hydroelectric plants, *Theoretical and Applied Climatology*,  
596 137, 353–371, <https://doi.org/10.1007/s00704-018-2600-8>, 2019.

597 Machado, L. A. T. and Rossow, W. B.: Structural Characteristics and Radiative Properties of Tropical Cloud Clusters, *Monthly*  
598 *Weather Review*, 121, 3234–3260, 1993.

599 Machado, L. A. T., Rossow, W. B., Guedes, R. L., and Walker, A. W.: Life cycle variations of mesoscale convective systems  
600 over the Americas, *Monthly Weather Review*, 126, 1630–1654, [https://doi.org/10.1175/1520-0493\(1998\)126<1630:LCVOMC>2.0.CO;2](https://doi.org/10.1175/1520-0493(1998)126<1630:LCVOMC>2.0.CO;2), 1998.

602 Marengo, J. A., Soares, W. R., Saulo, C., and Nicolini, M.: Climatology of the low-level jet east of the Andes as derived from  
603 the NCEP-NCAR reanalyses: Characteristics and temporal variability, *Journal of Climate*, 17, 2261–2280,  
604 [https://doi.org/10.1175/1520-0442\(2004\)017<2261:COTLJE>2.0.CO;2](https://doi.org/10.1175/1520-0442(2004)017<2261:COTLJE>2.0.CO;2), 2004.

605 Marengo, J. A., Ambrizzi, T., Alves, L. M., Barreto, N. J. C., Simões Reboita, M., and Ramos, A. M.: Changing Trends in  
606 Rainfall Extremes in the Metropolitan Area of São Paulo: Causes and Impacts, *Frontiers in Climate*, 2, 1–13,  
607 <https://doi.org/10.3389/fclim.2020.00003>, 2020.

608 Marengo, J. A., Camarinha, P. I., Alves, L. M., Diniz, F., and Betts, R. A.: Extreme Rainfall and Hydro-Geo-Meteorological  
609 Disaster Risk in 1.5, 2.0, and 4.0°C Global Warming Scenarios: An Analysis for Brazil, *Frontiers in Climate*, 3, 1–17,  
610 <https://doi.org/10.3389/fclim.2021.610433>, 2021.

611 Mehta, S., Mehta, S. K., Singh, S., Mitra, A., Ghosh, S. K., and Raha, S.: Characteristics of the Z–R Relationships Observed  
612 Using Micro Rain Radar (MRR-2) over Darjeeling (27.05° N, 88.26° E): A Complex Terrain Region in the Eastern Himalayas,  
613 *Pure and Applied Geophysics*, 177, 4521–4534, <https://doi.org/10.1007/s00024-020-02472-6>, 2020.

614 Moerman, J. W., Cobb, K. M., Adkins, J. F., Sodemann, H., Clark, B., and Tuen, A. A.: Diurnal to interannual rainfall  $\delta^{18}\text{O}$   
615 variations in northern Borneo driven by regional hydrology, *Earth and Planetary Science Letters*, 369–370, 108–119,  
616 <https://doi.org/10.1016/j.epsl.2013.03.014>, 2013.

617 Muller, C. L., Baker, A., Fairchild, I. J., Kidd, C., and Boomer, I.: Intra-Event Trends in Stable Isotopes: Exploring Midlatitude  
618 Precipitation Using a Vertically Pointing Micro Rain Radar, *Journal of Hydrometeorology*, 16, 194–213,  
619 <https://doi.org/10.1175/JHM-D-14-0038.1>, 2015.

620 Munksgaard, N. C., Kurita, N., Sánchez-Murillo, R., Ahmed, N., Araguas, L., Balachew, D. L., Bird, M. I., Chakraborty, S.,  
621 Kien Chinh, N., Cobb, K. M., Ellis, S. A., Esquivel-Hernández, G., Ganyaglo, S. Y., Gao, J., Gastmans, D., Kaseke, K. F.,  
622 Kebede, S., Morales, M. R., Mueller, M., Poh, S. C., Santos, V. dos, Shaoneng, H., Wang, L., Yacobaccio, H., and Zwart, C.:  
623 Data Descriptor: Daily observations of stable isotope ratios of rainfall in the tropics, *Scientific Reports*, 9, 1–7,  
624 <https://doi.org/10.1038/s41598-019-50973-9>, 2019.

625 R Core Team: A language and environment for statistical computing. R Foundation for Statistical Computing, Vienna, Austria.  
626 <https://www.R-project.org/>, 2023.

627 Rao, N. T., Kirankumar, N. V. P., Radhakrishna, B., and Rao, N. D.: Classification of tropical precipitating systems using  
628 wind profiler spectral moments. Part I: Algorithm description and validation, *Journal of Atmospheric and Oceanic Technology*,  
629 25, 884–897, <https://doi.org/10.1175/2007JTECHA1031.1>, 2008.

630 Ribeiro, B. Z., Machado, L. A. T., Biscaro, T. S., Freitas, E. D., Mozer, K. W., and Goodman, S. J.: An evaluation of the  
631 GOES-16 rapid scan for nowcasting in southeastern Brazil: Analysis of a severe hailstorm case, *Weather and Forecasting*, 34,  
632 1829–1848, <https://doi.org/10.1175/WAF-D-19-0070.1>, 2019.

633 Risi, C., Bony, S., and Vimeux, F.: Influence of convective processes on the isotopic composition ( $\delta^{18}\text{O}$  and  $\delta\text{D}$ ) of  
634 precipitation and water vapor in the tropics: 2. Physical interpretation of the amount effect, *Journal of Geophysical Research*  
635 *Atmospheres*, 113, 1–12, <https://doi.org/10.1029/2008JD009943>, 2008.

636 Risi, C., Bony, S., Vimeux, F., Chongd, M., and Descroix, L.: Evolution of the stable water isotopic composition of the rain  
637 sampled along Sahelian squall lines, *Quarterly Journal of the Royal Meteorological Society*, 136, 227–242,  
638 <https://doi.org/10.1002/qj.485>, 2010.

639 Risi, C., Galewsky, J., Reverdin, G., and Brient, F.: Controls on the water vapor isotopic composition near the surface of  
640 tropical oceans and role of boundary layer mixing processes, *Atmospheric Chemistry and Physics*, 19, 12235–12260,  
641 <https://doi.org/10.5194/acp-19-12235-2019>, 2019.

642 Roberts, R. D. and Rutledge, S.: Nowcasting storm initiation and growth using GOES-8 and WSR-88D data, *Weather and*  
643 *Forecasting*, 18, 562–584, [https://doi.org/10.1175/1520-0434\(2003\)018<0562:NSIAGU>2.0.CO;2](https://doi.org/10.1175/1520-0434(2003)018<0562:NSIAGU>2.0.CO;2), 2003.

644 Roca, R. and Fiolleau, T.: Extreme precipitation in the tropics is closely associated with long-lived convective systems,  
645 *Communications Earth & Environment*, 1, 18, <https://doi.org/10.1038/s43247-020-00015-4>, 2020.

646 Romatschke, U. and Houze, R. A.: Characteristics of precipitating convective systems accounting for the summer rainfall of  
647 tropical and subtropical South America, *Journal of Hydrometeorology*, 14, 25–46, <https://doi.org/10.1175/JHM-D-12-060.1>,  
648 2013.

649 Rozanski, K., Sonntag, C., and Munnich, K. O.: Factors controlling stable isotope composition of European precipitation.,  
650 *Tellus*, 34, 142–150, <https://doi.org/10.3402/tellusa.v34i2.10796>, 1982.

651 Rozanski, K., Araguás-Araguás, L., and Gonfiantini, R.: Isotopic Patterns in Modern Global Precipitation, 1–36,  
652 <https://doi.org/10.1029/GM078p0001>, 1993.

653 Salati, E., Dall'Olio, A., Matsui, E., and Gat, J. R.: Recycling of water in the Amazon Basin: An isotopic study, *Water*  
654 *Resources Research*, 15, 1250–1258, <https://doi.org/10.1029/WR015i005p01250>, 1979.

655 Sánchez-Murillo, R., Durán-Quesada, A. M., Birkel, C., Esquivel-Hernández, G., and Boll, J.: Tropical precipitation anomalies  
656 and d-excess evolution during El Niño 2014–16, *Hydrological Processes*, 31, 956–967, <https://doi.org/10.1002/hyp.11088>,  
657 2017.

658 Sánchez-Murillo, R., Durán-Quesada, A. M., Esquivel-Hernández, G., Rojas-Cantillano, D., Birkel, C., Welsh, K., Sánchez-  
659 Llull, M., Alonso-Hernández, C. M., Tetzlaff, D., Soulsby, C., Boll, J., Kurita, N., and Cobb, K. M.: Deciphering key processes  
660 controlling rainfall isotopic variability during extreme tropical cyclones, *Nature Communications*, 10, 1–10,

661 <https://doi.org/10.1038/s41467-019-12062-3>, 2019.

662 dos Santos, V., Gastmans, D., and Sánchez-Murillo, R.: Isotope and meteorologic database of high-frequency sampling of  
663 convective rainfall events in Rio Claro, Brazil, <https://doi.org/10.17632/kk3gs8zn4s.1>, 2023.

664 Sarkar, M., Bailey, A., Blossey, P., de Szoeko, S. P., Noone, D., Quiñones Meléndez, E., Leandro, M. D., and Chuang, P. Y.:  
665 Sub-cloud rain evaporation in the North Atlantic winter trade winds derived by pairing isotopic data with a bin-resolved  
666 microphysical model, *Atmospheric Chemistry and Physics*, 23, 12671–12690, <https://doi.org/10.5194/acp-23-12671-2023>,  
667 2023.

668 Schmit, T. J., Griffith, P., Gunshor, M. M., Daniels, J. M., Goodman, S. J., and Lebar, W. J.: A closer look at the ABI on the  
669 goes-r series, *Bulletin of the American Meteorological Society*, 98, 681–698, <https://doi.org/10.1175/BAMS-D-15-00230.1>,  
670 2017.

671 Shapiro, S. S.; Wilk, M. B.: An analysis of variance test for normality (complete samples), *Biometrika*, 53, 591–611, 1965.

672 Siqueira, J. R. and Machado, L. A. T.: Influence of the frontal systems on the day-to-day convection variability over South  
673 America, *Journal of Climate*, 17, 1754–1766, [https://doi.org/10.1175/1520-0442\(2004\)017<1754:IOTFSO>2.0.CO;2](https://doi.org/10.1175/1520-0442(2004)017<1754:IOTFSO>2.0.CO;2), 2004.

674 Siqueira, J. R., Rossow, W. B., Machado, L. A. T., and Pearl, C.: Structural characteristics of convective systems over South  
675 America related to cold-frontal incursions, *Monthly Weather Review*, 133, 1045–1064, <https://doi.org/10.1175/MWR2888.1>,  
676 2005.

677 Soderberg, K., Good, S. P., O’connor, M., Wang, L., Ryan, K., and Caylor, K. K.: Using atmospheric trajectories to model the  
678 isotopic composition of rainfall in central Kenya, *Ecosphere*, 4, 1–18, <https://doi.org/10.1890/ES12-00160.1>, 2013.

679 Stein, A. F., Draxler, R. R., Rolph, G. D., Stunder, B. J. B., Cohen, M. D., and Ngan, F.: Noaa’s hysplit atmospheric transport  
680 and dispersion modeling system, *Bulletin of the American Meteorological Society*, 96, 2059–2077,  
681 <https://doi.org/10.1175/BAMS-D-14-00110.1>, 2015.

682 Steiner, M. and Smith, J. A.: Convective versus stratiform rainfall: An ice-microphysical and kinematic conceptual model,  
683 *Atmospheric Research*, 47–48, 317–326, [https://doi.org/10.1016/S0169-8095\(97\)00086-0](https://doi.org/10.1016/S0169-8095(97)00086-0), 1998.

684 Stewart, M. K.: Stable isotope fractionation due to evaporation and isotopic exchange of falling waterdrops: Applications to  
685 atmospheric processes and evaporation of lakes, *Journal of Geophysical Research*, 80, 1133–1146,  
686 <https://doi.org/10.1029/JC080i009p01133>, 1975.

687 Sun, C., Shanahan, T. M., and Partin, J.: Controls on the isotopic composition of precipitation in the South-Central United  
688 States, *Journal of Geophysical Research: Atmospheres*, 124, 8320–8335, <https://doi.org/10.1029/2018JD029306>, 2019.

689 Sun, C., Tian, L., Shanahan, T. M., Partin, J. W., Gao, Y., Piatrunia, N., and Banner, J.: Isotopic variability in tropical cyclone  
690 precipitation is controlled by Rayleigh distillation and cloud microphysics, *Communications Earth & Environment*, 3,  
691 <https://doi.org/10.1038/s43247-022-00381-1>, 2022.

692 Taupin, J.-D., Gallaire, R., and Arnaud, Y.: Analyses isotopiques et chimiques des précipitations sahélienne de la région de  
693 Niamey au Niger: implications climatologiques, *Hydrochemistry*, 151–162, 1997.

694 Torri, G.: On the isotopic composition of cold pools in radiative-convective equilibrium, *Journal of Geophysical Research*:

695 Atmospheres, 126, 1–20, <https://doi.org/10.1029/2020JD033139>, 2021.

696 Tremoy, G., Vimeux, F., Soumana, S., Souley, I., Risi, C., Favreau, G., and Oï, M.: Clustering mesoscale convective systems  
697 with laser-based water vapor  $\delta^{18}\text{O}$  monitoring in Niamey (Niger), *Journal of Geophysical Research: Atmospheres*, 119, 5079–  
698 5103, <https://doi.org/10.1002/2013JD020968>, 2014.

699 Vila, D. A., Machado, L. A. T., Laurent, H., and Velasco, I.: Forecast and tracking the evolution of cloud clusters (ForTraCC)  
700 using satellite infrared imagery: Methodology and validation, *Weather and Forecasting*, 23, 233–245,  
701 <https://doi.org/10.1175/2007WAF2006121.1>, 2008.

702 de Vries, A. J., Aemisegger, F., Pfahl, S., and Wernli, H.: Stable water isotope signals in tropical ice clouds in the West African  
703 monsoon simulated with a regional convection-permitting model, *Atmospheric Chemistry and Physics*, 22, 8863–8895,  
704 <https://doi.org/10.5194/acp-22-8863-2022>, 2022.

705 World Meteorological Organization: WMO Atlas of Mortality and Economic Losses From Weather , Climate and Water  
706 Extremes (1970-2019), Geneva 2, Switzerland, 90 pp., 2021.

707 Zawadzki, I. and Antonio, M. D. A.: Equilibrium Raindrop Size Distributions in Tropical Rain, *Journal of the Atmospheric*  
708 *Sciences*, 45, 3452–3459, [https://doi.org/10.1175/1520-0469\(1988\)045<3452:ERSDIT>2.0.CO;2](https://doi.org/10.1175/1520-0469(1988)045<3452:ERSDIT>2.0.CO;2), 1988.

709 Zilli, M. T., Carvalho, L. M. V., Liebmann, B., and Silva Dias, M. A.: A comprehensive analysis of trends in extreme  
710 precipitation over southeastern coast of Brazil, *International Journal of Climatology*, 37, 2269–2279,  
711 <https://doi.org/10.1002/joc.4840>, 2017.

712 Zwart, C., Munksgaard, N. C., Protat, A., Kurita, N., Lambrinidis, D., and Bird, M. I.: The isotopic signature of monsoon  
713 conditions, cloud modes, and rainfall type, *Hydrological Processes*, 32, 2296–2303, <https://doi.org/10.1002/hyp.13140>, 2018.

714

715

716

717

**Table 1.** Summarizing overall convective rainfall events, isotope and meteorological parameters

Season		Spring		Autumn			Summer		
Data		2019/11/05	2020/11/18	2020/05/23	2020/06/09	2020/01/30	2020/02/10	2020/02/01	2021/02/24
<b>Number of samples</b>		21	8	4	12	6	18	5	16
<b>Duration</b>		82	141	131	96	23	86	18	55
<b><math>\delta^{18}\text{O}</math></b>	<b>Initial</b>	-3.0	-2.7	-2.6	-3.6	-10.1	-12.3	-10.2	-7.6
	<b>Median</b>	-3.1	-4.2	-2.9	-3.4	-10	-13.9	-10.4	-6.8
	<b><math>\Delta\delta</math></b>	2.4	2.6	0.8	2.2	1.1	7.3	1.5	3.5
<b><math>\delta^2\text{H}</math></b>	<b>Initial</b>	3.4	-4.6	-4.6	-5.2	-60.1	-86.6	-71.0	-47.8
	<b>Median</b>	0.8	-13.7	-6.9	-5.6	-64.4	-92.0	-73.5	-44.8
	<b><math>\Delta\delta</math></b>	16.9	9.9	8.9	11	10.5	43.1	7.4	20.9
<b><i>d</i>-excess</b>	<b>Initial</b>	27.4	10.2	16.7	24.1	20.8	12.1	11.3	13.0
	<b>Median</b>	22.9	19.7	16.3	17.3	15.7	17.5	13.4	7.2
	<b><math>\Delta\delta</math></b>	7.1	12.8	4.0	19.2	9.5	16.6	8.4	17.2
<b>Automatic Weather Station</b>	<b>Rain rate</b>	0.4	0.2	0.1	0.3	0.4	0.5	0.6	0.5
	<b>RH</b>	96	85	87	95	93	97	93	86
	<b>T</b>	21	20	19	19	23	22	23	21
	<b>Tdw</b>	20	17	17	18	21	21	21	18
	<b>LCL</b>	146	489	449	168	247	93	253	468
<b>Micro Rain Radar</b>	<b>Zc</b>	46	38	33	42	38	41	39	35
	<b>w</b>	8	7.1	6.6	7.7	6.6	6.7	7.1	7.1
<b>GOES-16</b>	<b>BT</b>	-63	-63	-56	-50	-53	-39	-60	-51

720 Duration (minutes); Isotopes parameters (‰); Median values of meteorological variables: Rain rate ( $\text{mm}\cdot\text{min}^{-1}$ ), Relative Humidity – (RH %), Temperature (T °C), Dew Temperature (Tdw °C), Lifting Condensation Level (LCL meters), Reflectivity (Zc dBZ), Vertical Velocity ( $\text{m}\cdot\text{s}^{-1}$ ) and Brightness temperature (BT °C).



**Table 2.** The results of semi-quantitative assessment of the impact of below-cloud processes on the isotope characteristics of convective precipitation

Rainfall event	T <sub>INT</sub> <sup>a)</sup> (°C)	RH <sub>INT</sub> <sup>b)</sup> (%)	F <sup>c)</sup> (-)	▲ d-excess <sup>d)</sup> (‰)
<u>The 2019/11/05 event</u> δ <sub>o</sub> - isotopic composition of rainfall (‰): δ <sup>2</sup> H = 0.80, δ <sup>18</sup> O = -3.11, <i>d</i> -excess = 25.7 δ <sub>A</sub> – isotopic composition of equilibrium vapour (‰) <sup>e)</sup> : δ <sup>2</sup> H = -78.3 δ <sup>18</sup> O = -12.84, <i>d</i> -excess = 24.4	19.3	97.8	0.9982	1.7
<u>The 2020/11/18</u> δ <sub>o</sub> - isotopic composition of rainfall (‰): δ <sup>2</sup> H = -13.7, δ <sup>18</sup> O = -4.16, <i>d</i> -excess = 19.5 δ <sub>A</sub> – isotopic composition of equilibrium vapour (‰): δ <sup>2</sup> H = -93.2 δ <sup>18</sup> O = -14.01, <i>d</i> -excess = 18.8	19.0	92.9	0.9795	3.1
<u>The 2020/05/23</u> δ <sub>o</sub> - isotopic composition of rainfall (‰): δ <sup>2</sup> H = -6.9, δ <sup>18</sup> O = -2.89, <i>d</i> -excess = 16.2 δ <sub>A</sub> – isotopic composition of equilibrium vapour (‰): δ <sup>2</sup> H = -86.6 δ <sup>18</sup> O = -12.72, <i>d</i> -excess = 15.2	18.1	93.4	0.9806	2.8
<u>The 2020/06/09</u> δ <sub>o</sub> - isotopic composition of rainfall (‰): δ <sup>2</sup> H = -5.5, δ <sup>18</sup> O = -3.37, <i>d</i> -excess = 21.3 δ <sub>A</sub> – isotopic composition of equilibrium vapour (‰): δ <sup>2</sup> H = -84.8 δ <sup>18</sup> O = -13.15, <i>d</i> -excess = 20.4	19.3	97.5	0.9978	0.2
<u>The 2020/01/30</u> δ <sub>o</sub> - isotopic composition of rainfall (‰): δ <sup>2</sup> H = -64.4, δ <sup>18</sup> O = -10.03, <i>d</i> -excess = 15.8 δ <sub>A</sub> – isotopic composition of equilibrium vapour (‰) <sup>e)</sup> : δ <sup>2</sup> H = -135.5 δ <sup>18</sup> O = -19.44, <i>d</i> -excess = 20.0	22.4	96.4	0.9944	0.9
<u>The 2020/02/10</u> δ <sub>o</sub> - isotopic composition of rainfall (‰): δ <sup>2</sup> H = -91.97, δ <sup>18</sup> O = -13.85, <i>d</i> -excess = 18.8 δ <sub>A</sub> – isotopic composition of equilibrium vapour (‰) <sup>e)</sup> : δ <sup>2</sup> H = -161.6 δ <sup>18</sup> O = -23.28, <i>d</i> -excess = 24.6	21.7	98.6	0.9994	0.1
<u>The 2020/02/01</u> δ <sub>o</sub> - isotopic composition of rainfall (‰): δ <sup>2</sup> H = -73.5, δ <sup>18</sup> O = -10.44, <i>d</i> -excess = 10.2 δ <sub>A</sub> – isotopic composition of equilibrium vapour (‰) <sup>e)</sup> : δ <sup>2</sup> H = -143.8 δ <sup>18</sup> O = -19.80, <i>d</i> -excess = 14.6	22.5	96.3	0.9947	0.9
<u>The 2021/02/24</u> δ <sub>o</sub> - isotopic composition of rainfall (‰): δ <sup>2</sup> H = -44.8, δ <sup>18</sup> O = -6.79, <i>d</i> -excess = 9.5 δ <sub>A</sub> – isotopic composition of equilibrium vapour (‰): δ <sup>2</sup> H = -120.3 δ <sup>18</sup> O = -16.48, <i>d</i> -excess = 11.5	19.3	93.2	0.9800	3.0

a) mean temperature of below cloud ambient atmosphere (linear interpolation between cloud base and ground level values)

- 725 b) mean relative humidity of below cloud ambient atmosphere (linear interpolation between cloud base and ground level values)  
c) remaining mass fraction of raindrops after their travel from the cloud base to the surface (see text)  
d) reduction of the  $d$ -excess of raindrops as a result of their travel from the cloud base to the surface (see text)  
e) assumed isotopic composition of ambient humid atmosphere below the cloud base derived from the measured isotopic composition of rainfall and ground-level temperature.

730

735

740

745

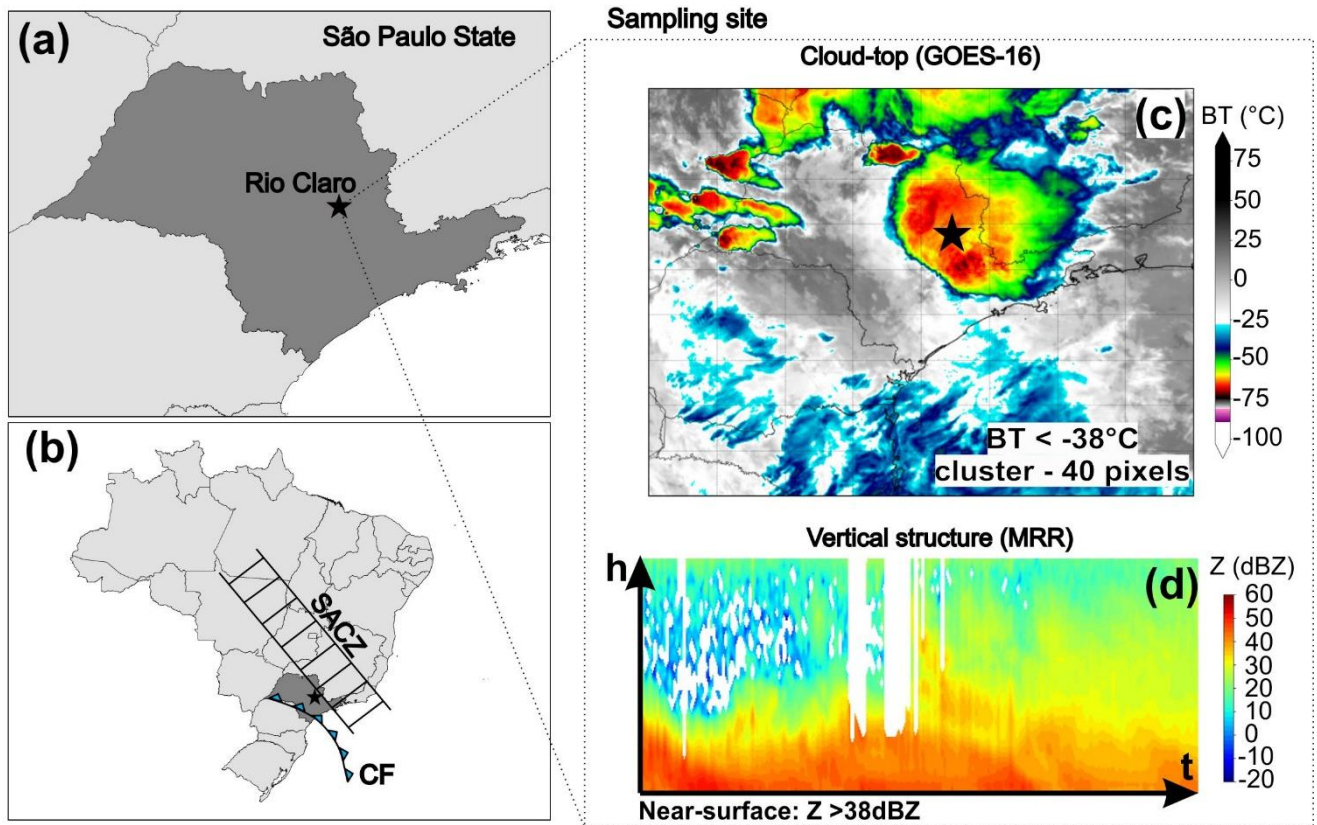


**Figure 1.** Regional and local context of study area. (a) Localization of sampling site in Rio Claro (black star) (b) regional synoptic context across Brazil and main weather systems (CF – cold front and SACZ – Southern Atlantic Convergence Zone). (c) GOES-16 satellite imagery of convective rainfall (d) Micro Rain Radar (MRR) image of convective rainfall.

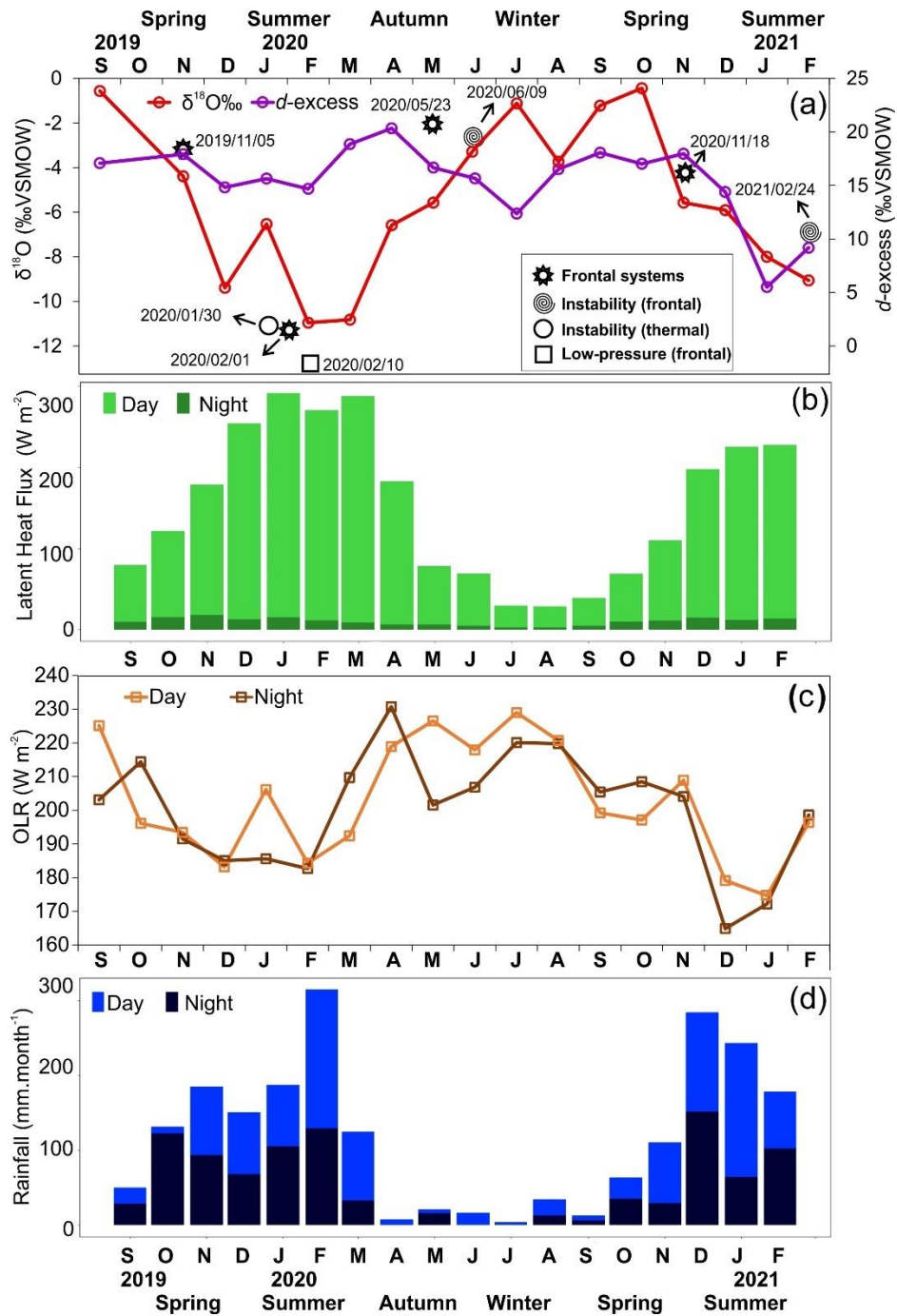
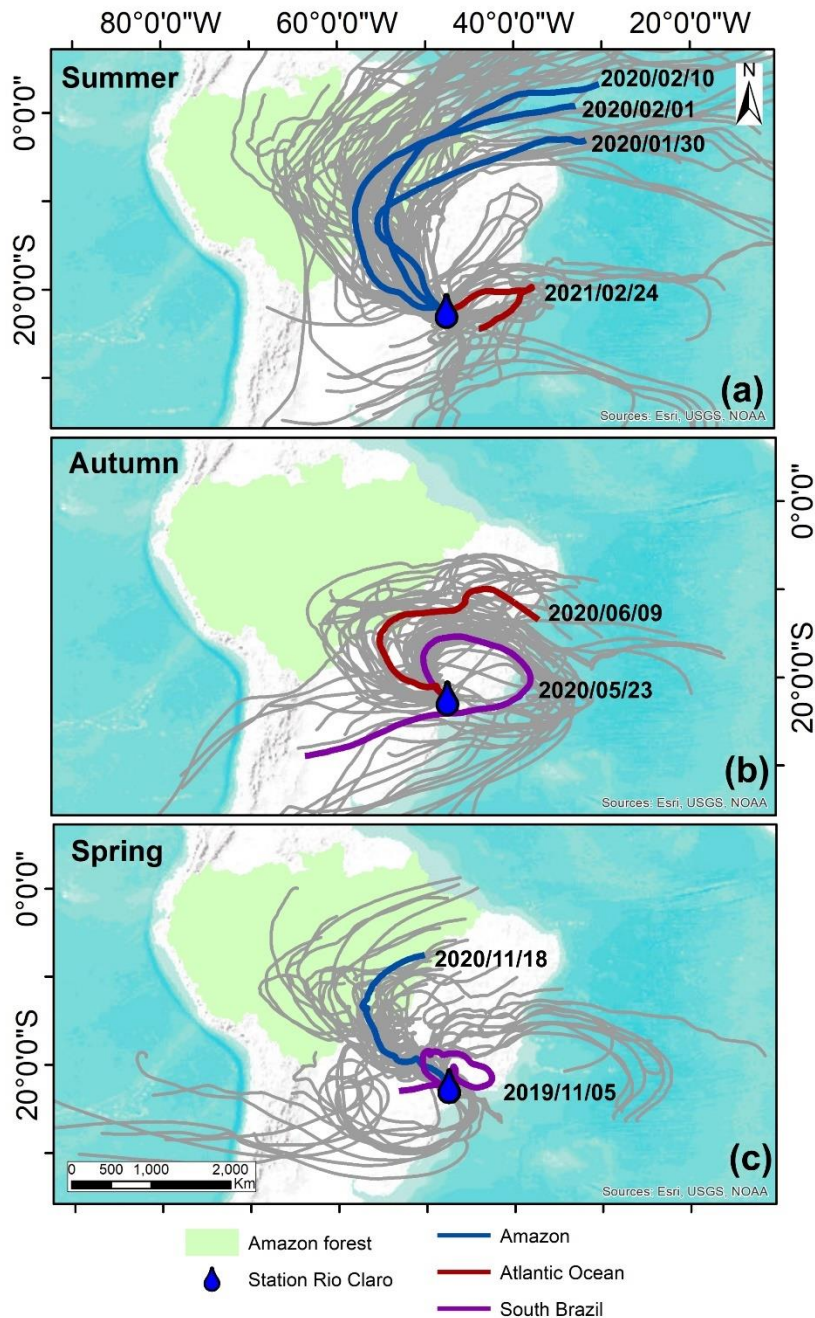


**Figure 2.** Seasonal variation of isotope and convective parameters. (a) Temporal distribution of monthly  $\delta^{18}\text{O}$  and  $d$ -excess values during study period, with aggregated median of  $\delta^{18}\text{O}$  values for high-frequency convective rainfall events (b) AQUA/AIRS latent heat flux. (c) MERRA-2 outgoing longwave radiation (monthly averaged daytime and night-time data) (d) monthly rainfall amounts at Rio Claro separated into day and night fraction (no rainfall types distinguished). The black symbol indicates weather systems described in section 3.1. The monthly isotopic composition used in this figure was collected by the first authors of the article and determined by the UNESP laboratory, following the same procedures mentioned in section 2.2.



760 **Figure 3.** Ten-day backward trajectories arriving at Rio Claro station of eight convective events. (a) Summer, (b) Autumn and (c) Spring. Twenty-seven ensembles are grey lines, and the mean trajectory is the colors lines. The colours of the mean trajectories indicate the origin of air masses. The authors used trivial information, the borders of the countries and the ocean provided by the ESRI base map.

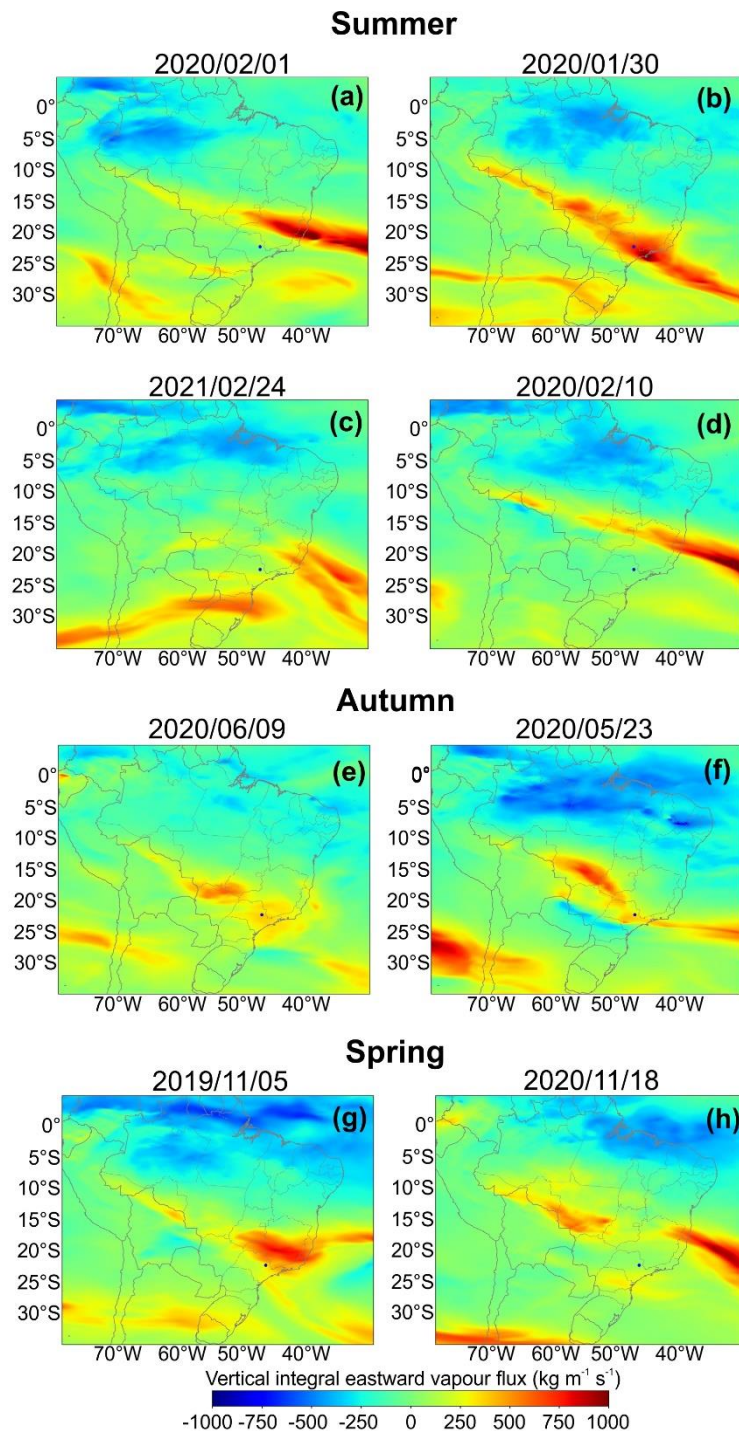


**Figure 4.** ERA-5 vertical integral of eastward water vapor flux. (a, b, c, d) summer convective events (e, f) autumn and (g, h) spring aggregated. The maps corresponded to the days when convective rainfall events occurred. Positive values indicate the direction of moisture vapor flux from left to right, and negative values from right to left.

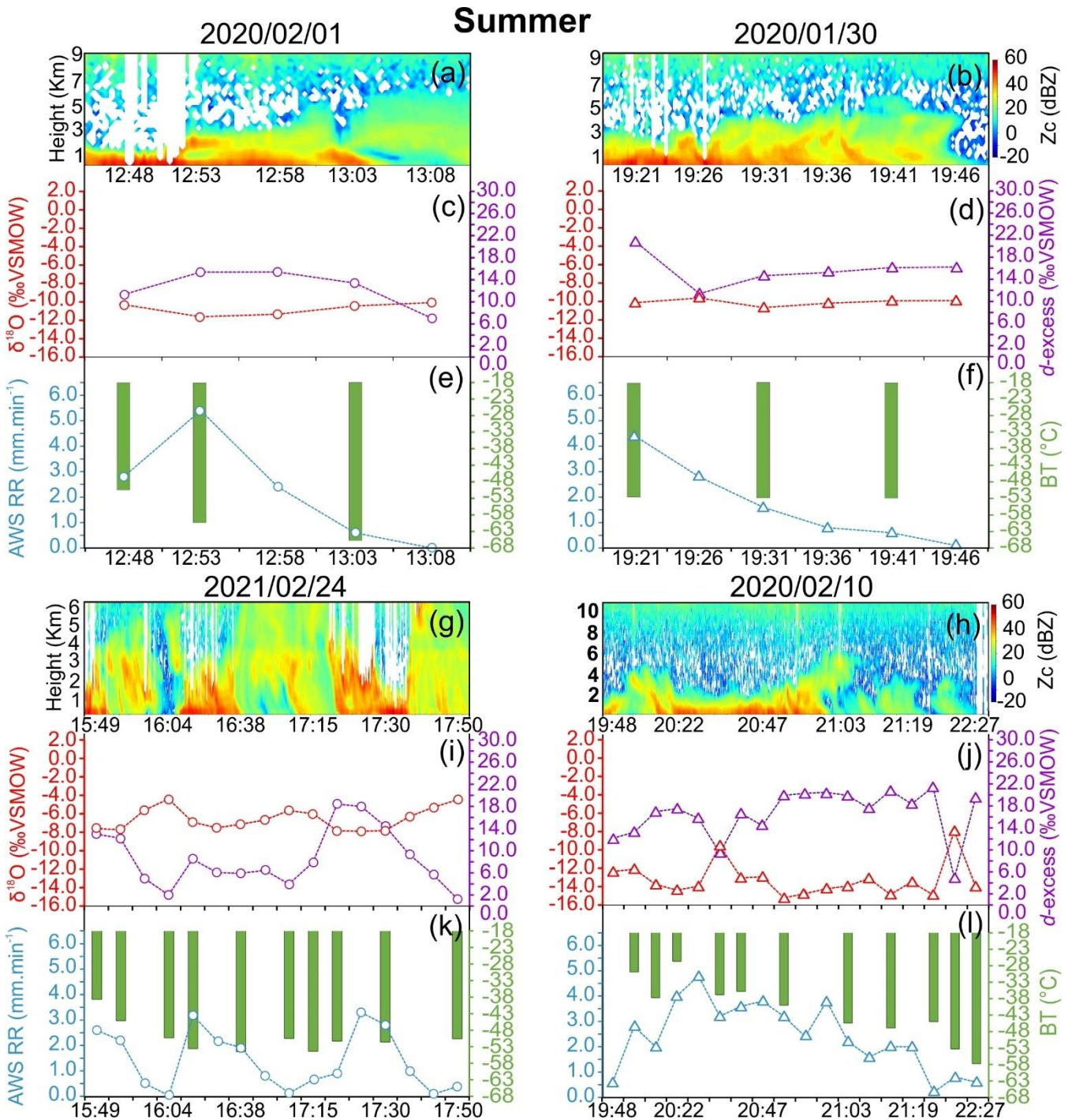


**Figure 5.** Summer intra-events. (a, b, g, h) radar reflectivity of Micro Rain Radar (c, d, i, j)  $\delta^{18}\text{O}$  (red lines) and  $d$ -excess (purple lines) (e, f, k, l) brightness temperature (BT – green bars) and rainfall amount (blue lines).

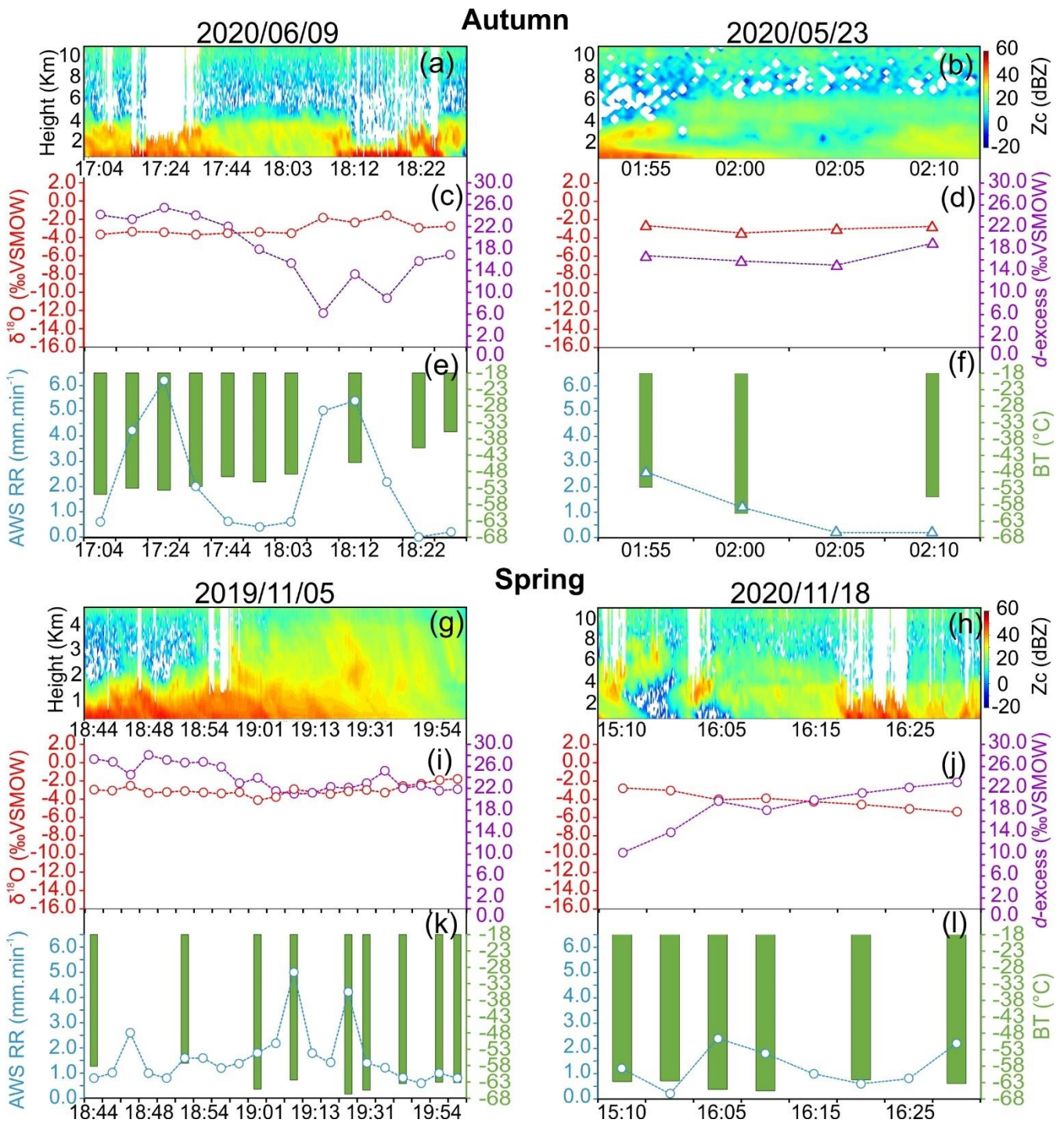


**Figure 6.** Autumn and spring intra-events. Refer to Fig. 5 for legend description.